

Geochemistry, Geophysics, Geosystems

RESEARCH ARTICLE

10.1029/2019GC008489

This article is a companion to Tian et al. (2019), <https://doi.org/10.1029/2019GC008488>.

Key Points:

- Up-slab fluid flow is necessary to form a flux peak at subarc depths
- Serpentine dehydration can redistribute CO₂ from slab interior to capping sediments
- Sediment removal from slab top promotes slab CO₂ release

Correspondence to:

M. Tian,
meng.tian@csh.unibe.ch

Citation:

Tian, M., Katz, R. F., Rees Jones, D. W., & May, D. A. (2019). Devolatilization of Subducting Slabs, Part II: Volatile Fluxes and Storage. *Geochemistry, Geophysics, Geosystems*, 20, 6199–6222. <https://doi.org/10.1029/2019GC008489>





Received 7 JUN 2019

Accepted 24 NOV 2019

Accepted article online 26 NOV 2019

Published online 28 DEC 2019

Devolatilization of Subducting Slabs, Part II: Volatile Fluxes and Storage

Meng Tian^{1,2} , Richard F. Katz¹ , David W. Rees Jones^{1,3,4} , and Dave A. May¹ 

¹Department of Earth Sciences, University of Oxford, Oxford, UK, ²Center for Space and Habitability, University of Bern, Bern, Switzerland, ³Department of Earth Sciences, Bullard Laboratories, University of Cambridge, Cambridge, UK, ⁴School of Mathematics and Statistics, University of St Andrews, St Andrews, UK

Abstract Subduction is a crucial part of the long-term water and carbon cycling between Earth's exosphere and interior. However, there is broad disagreement over how much water and carbon is liberated from subducting slabs to the mantle wedge and transported to island-arc volcanoes. In the Tian et al. (2019) Part I, we parameterize the metamorphic reactions involving H₂O and CO₂ for representative subducting lithologies. On this basis, a two-dimensional reactive transport model is constructed in this Part II. We assess the various controlling factors of CO₂ and H₂O release from subducting slabs. Model results show that up-slab fluid flow directions produce a flux peak of CO₂ and H₂O at subarc depths. Moreover, infiltration of H₂O-rich fluids sourced from hydrated slab mantle enhances decarbonation or carbonation at lithological interfaces, increases slab surface fluxes, and redistributes CO₂ from basalt and gabbro layers to the overlying sedimentary layer. As a result, removal of the cap sediments (by diapirism or off-scraping) leads to elevated slab surface CO₂ and H₂O fluxes. The modeled subduction efficiency (the percentage of initially subducted volatiles retained until ~200 km deep) of H₂O and CO₂ is increased by open-system effects due to fractionation within the interior of lithological layers.

1. Introduction

Earth distinguishes itself from other solar system planets through its habitability that is maintained by its surface climate. Over geological time, water and carbon modulate the climate through geochemical cycles between Earth's exosphere and interior (Dasgupta et al., 2013). Subduction is a tectonic process that brings altered, near-surface rock into the deep Earth and therefore participates in the long-term geochemical cycles. However, the flux of carbon accompanying subduction into deep Earth is still actively debated. Dasgupta and Hirschmann (2010) and Hirschmann (2018) argue that subducting slabs do not experience significant degassing or partial melting and so sequester their carbon into the deep Earth over geological history. On the other hand, Kelemen and Manning (2015) contend that most carbon is liberated from slabs and migrates into the subduction zone mantle lithosphere, rather than being recycled into the deep mantle.

Detailed field and modeling studies also give disparate views on the fate of subducting carbon. Kerrick and Connolly (1998, 2001a, 2001b) used thermodynamics to construct petrological phase diagrams for representative lithologies in subduction zones (i.e., hydrothermally altered slab mantle, metabasalts, metasediments). They concluded that all representative lithologies bring a significant amount of CO₂ into the deep mantle, except that clay-rich slab sediments undergo complete decarbonation at forearc depths along hot subduction geotherms. Subsequently, Gorman et al. (2006) evaluated the open-system effects induced by aqueous fluid infiltration on the thermodynamic modeling of subduction zone dehydration and decarbonation. They concluded that CO₂ liberation is still limited, in spite of H₂O-rich fluid infiltration. Field studies on subducted carbonates, however, suggest considerable carbon release by carbonate dissolution (Ague and Nicolescu, 2014; Frezzotti et al., 2011); Piccoli et al. (2016) show that the dissolved carbon can be reprecipitated within the slab or proximal mantle wedge. Further thermodynamic models considering aqueous ionic species also suggest that carbon release from subducting slabs is significant because dissolution of carbon in the form of organic ions can enhance carbon removal from rocks (Sverjensky et al., 2014). In particular, Connolly and Galvez (2018) show that consideration of nonmolecular species can roughly double the carbon solubility in fluids coexisting with sediments subducted along cool geotherms.

Purely thermodynamic models of the fate of subducted carbon are zero dimensional in that the system is assumed to be closed, with no directional mass transfer. In contrast, the one-dimensional, open-system model by Gorman et al. (2006) treated H_2O and CO_2 allowing for vertical fluid migration. Two-dimensional geodynamic models of porous fluid migration indicates substantial fluid migration nearly parallel to subducting slabs (Wilson et al., 2014). This focused flow is caused by the formation of a high-permeability channel in the dewatering layer and a compaction pressure gradient that helps contain liquids in the slab. Given that flow directions within the slab are uncertain and reactive flow is path-dependent, it is important to assess the effect of fluid flow direction on the fluxes of H_2O and CO_2 out of subducting slabs.

In the computational treatment of open-system behaviors, an extra challenge exists when incorporating metamorphic reactions involving volatiles into fluid flow modeling. Since fluid movement constantly changes the bulk composition of each subdomain within the modeled slab, the computational cost may be prohibitively high if a traditional phase diagram calculation is applied to each subdomain repeatedly throughout the model evolution. In the Tian et al. (2019) Part I, we have parameterized the coupled dehydration and decarbonation processes for representative subducting lithologies (i.e., sediments, mid-ocean ridge basalt [MORB], gabbro, and peridotite). This light-weight thermodynamic module focuses on the behaviors of H_2O and CO_2 and can readily capture the fractionation and infiltration effects typical in open systems. Thus, it forms the basis of the efficient reactive flow model in the current study. We note here that the liquid volatile phase in the model is a molecular fluid residing in the H_2O – CO_2 binary, so it excludes other carbon species from consideration. The limitation of this assumption is discussed in section 5 and in the Tian et al. (2019) Part 1.

In this paper, we provide a two-dimensional model of reactive fluid flow in subducting slabs. Since the dynamics of within-slab flow remains highly uncertain (Faccenda et al., 2009; Morishige and van Keken, 2018; Plümper et al., 2017; Wilson et al., 2014), we prescribe the flow direction in our model and investigate model behavior as a function of this parameter, rather than solving equations for momentum conservation. The model incorporates open-system equilibrium thermodynamics and enables us to assess the factors controlling slab dehydration and decarbonation. In particular, we find that nearly up-slab fluid flow produces a peak in the volatile flux at subarc depths and might thus be relevant for arc magmatism. We find that a sedimentary layer can act as a cap that absorbs CO_2 released from underlying slab lithologies, if the sediments are not removed during subduction. Furthermore, slab lithospheric mantle, if extensively serpentinized, can cause significant H_2O and CO_2 fluxes at subarc depths in warm subduction settings. In all the cases we explored, 20–90 wt% H_2O and 80–100 wt% CO_2 in the slabs subduct beyond a mantle depth of ~ 200 km.

In the following, we start with a description of our model setup in section 2, followed by the numerics of model solution in section 3. Model results with closed-system behavior are presented in section 4.1, which is included to facilitate comparison of our model with previous work assuming constant bulk compositions. We present results on a reference, open-system model in section 4.2, both for comparison with the closed-system model and to serve as a reference case to investigate parameter sensitivity. The subsequent models presented explore the variability of H_2O and CO_2 fluxes on slab surface in response to changes in fluid flow direction (section 4.3), slab age (section 4.4), extent of slab mantle serpentinization (section 4.5), and removal of slab surface sediments (section 4.6). For all the open-system models we run, the efficiency of H_2O and CO_2 subduction into the deep mantle is summarized in section 4.7, which is followed by a discussion (section 5) of the model limitations.

2. Model Setup

The geometry of the model is illustrated in Figure 1; we focus only on the subducting slab. Cold temperatures in the slab create strong resistance to viscous (de-)compaction (Wilson et al., 2014) and hence the slab experiences negligible isotropic deformation over the model times in this study (~ 6 Ma). We therefore treat the slab as a rigid plate in our model. Slab deformation has also been modeled using viscoelastic (Morishige and van Keken, 2018) and visco-elasto-plastic rheologies (Gerya, 2011), yielding diverse fluid flow patterns within slab. By treating the slab as a rigid plate, the flow direction can be considered as a free parameter that is to be explored (see below), and we can thus circumvent the uncertainties of slab deformation and coupled fluid flow that are difficult to constrain.

Under the rigid plate assumption, the solid velocities (v_s) in the slab are uniformly of magnitude equal to the subduction rate and can be prescribed as a model parameter. If a slab age and dip are further chosen,

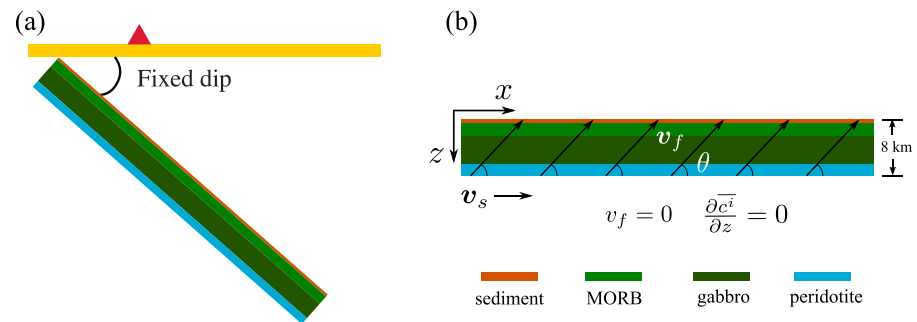


Figure 1. Sketch showing the model geometry and boundary conditions. (a) The geodynamic setting of our model. It shows that the model assumes a fixed slab dipping angle and the slab acts like a rigid plate that does not deform. A red triangle denotes the position of arc volcano. (b) The modeled slab domain. The x and z axes are respectively parallel and normal to the slab extension; this coordinate system is used in all the succeeding figures displaying the entire slab. The slab lithologically consists of four representative rock types as detailed in the legend. Solid velocities within the slab are uniformly set to slab convergence rate (v_s). θ is the angle between the x -axis and the uniform fluid flow direction. Notations of symbols are listed in Table 1 and details on the initial and boundary conditions are provided in section 3.

the steady-state temperature (T) and pressure (P) of the slab can be calculated using canonical thermomechanical models (van Keken et al., 2008). Our model assumes such a steady-state P - T structure of the slab and extracts it from the geodynamic model by England and Katz (2010). Figure 2 illustrates an example of this for a 10 Ma slab with a convergence rate of 5 cm/yr and a dip of 45° . This P - T field is employed in the following sections except section 4.4 where different thermal structures, dependent on slab age, are tested. Note that this is a young, warm, and relatively fast-converging oceanic lithosphere. The relatively fast subduction speed implies a fast-spreading rate at mid-ocean ridges, which correlates with small extent of upper mantle serpentinization (Früh-Green et al., 2004). The chosen H_2O content of 1 wt% for the modeled slab mantle is thus consistent with this spreading rate.

Superimposed on this rigid and thermally steady-state slab is the reactive H_2O and CO_2 transport model. This transport model assumes local equilibrium between the solid and percolating liquid phases. The solid phase in the slab is lithologically layered, as shown in Figure 1b and consists of sediments, MORBs, gabbros, and peridotites from top to bottom. In the Tian et al. (2019) Part I, we parameterize the equilibrium partitioning of H_2O and CO_2 between the liquid and solid for each of the four representative lithologies; this parameterization serves as a thermodynamic module coupled to the fluid flow model detailed below.

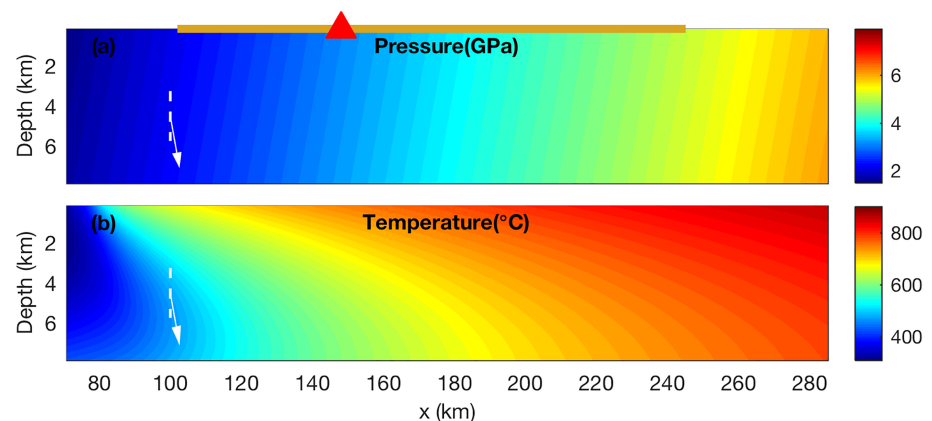


Figure 2. A representative illustration of the (a) P and (b) T structure for a 10 Ma slab. A convergence rate of 5 cm/yr and a slab dip of 45° are used. The x -axis starts from ~ 70 km because we assume that the overriding plate (Figure 1) has a 50-km-thick lithosphere which corresponds to ~ 70 km for the starting position of the slab immediately below it. The solid brown line in (a) draws the global range of arc positions projected onto slab surface (Syracuse and Abers, 2006), and the red triangle marks the site of the average position (~ 150 km); the same convention is used in the following figures. Note that the vertical and horizontal scales are different due to the high aspect ratio of the modeled slab. White dashed lines are a reference direction perpendicular to slab extension and solid white arrows denote the direction of gravity in the stretched domain; the same line and arrow conventions apply in the succeeding figures.

Table 1
Notations of Symbols

Symbol	Meaning	Unit
D	diffusion coefficient of CO ₂ or H ₂ O	$\sim 10^{-8}$ m/s ²
P	pressure	GPa
T	temperature	°C
H	slab thickness	m
i	H ₂ O or CO ₂	
t	time	s
x	coordinate along slab	m
z	coordinate normal to slab	m
θ	uniform flow angle	
ϕ	porosity	
v_f	fluid velocity	m/s
v_f	magnitude of fluid velocity	m/s
v_s	solid velocity	m/s
v_s	subduction rate	m/s
ρ_f	fluid phase density	kg/m ³
ρ_s	solid phase density	kg/m ³
c_f^i	mass fraction of i in fluid phase	
c_s^i	mass fraction of i in solid phase	
\bar{c}^i	bulk content of i per unit rock volume	kg/m ³
\bar{c}_{th}^i	bulk mass fraction of i	
Γ	reaction rate	kg/m ³ /s ¹
Γ_i	reaction rate for i	kg/m ³ /s ¹

Following previous studies (McKenzie, 1984; Katz, 2008; Keller and Katz, 2016; Scott and Stevenson, 1986), mass conservation for liquid and solid phases in porous media are expressed as

$$\frac{\partial \phi}{\partial t} + \nabla \cdot (\mathbf{v}_f \phi) = \frac{\Gamma}{\rho_f}, \quad (1)$$

$$\frac{\partial (1 - \phi)}{\partial t} + \nabla \cdot [\mathbf{v}_s (1 - \phi)] = -\frac{\Gamma}{\rho_s}, \quad (2)$$

where densities of both phases are assumed to be constant, and the meaning of the symbols is listed in Table 1. In addition, the conservation of volatile species H₂O and CO₂ in both phases are

$$\frac{\partial (\rho_f \phi c_f^i)}{\partial t} + \nabla \cdot (\rho_f \mathbf{v}_f \phi c_f^i) = \Gamma_i, \quad (3)$$

$$\frac{\partial [\rho_s (1 - \phi) c_s^i]}{\partial t} + \nabla \cdot [\rho_s \mathbf{v}_s (1 - \phi) c_s^i] = -\Gamma_i, \quad (4)$$

where i represents either H₂O or CO₂. Chemical diffusion is neglected here because the Péclet number ($v_f H/D$) is ~ 250 if slab thickness (H) of 8 km, diffusion coefficient (D) of $\sim 10^{-8}$ m²/s, porosity (ϕ) of $\sim 10^{-2}$ (e.g., Figure 4g), and a very conservative flux ($v_f \phi$) estimate of ~ 0.1 m/kyr (e.g., Figure 4h) are used. Adding equation (1) to equation (2) and equation (3) to (4) leads respectively to

$$-(\rho_s - \rho_f) \frac{\partial \phi}{\partial t} + \rho_f \nabla \cdot (\mathbf{v}_f \phi) = \rho_s \mathbf{v}_s \cdot \nabla \phi, \quad (5)$$

$$\frac{\partial [\rho_f \phi c_f^i + \rho_s (1 - \phi) c_s^i]}{\partial t} + \rho_f \nabla \cdot [\phi \mathbf{v}_f c_f^i] + \rho_s \mathbf{v}_s \cdot \nabla [(1 - \phi) c_s^i] = 0. \quad (6)$$

Note that, in deriving equations (5) and (6), the zero-compaction-rate assumption ($\nabla \cdot \mathbf{v}_s = 0$) is used, consistent with equation (7) below.

In the coordinate system where the x -axis is parallel to and the z -axis is normal to the slab extension, if the angle of flow direction (θ) is uniform across the slab (Figure 1b), then \mathbf{v}_s and \mathbf{v}_f in 2-D can be written as

$$\begin{aligned}\mathbf{v}_s &= (v_s, 0), \\ \mathbf{v}_f &= v_f(\cos \theta, \sin \theta),\end{aligned}\quad (7)$$

where v_s is the subduction rate, v_f is the magnitude of fluid velocity, and θ represents flow direction, a model parameter that will be explored in section 4. Substituting equation (7) into equations (5) and (6) yields

$$-(\rho_s - \rho_f) \frac{\partial \phi}{\partial t} + \rho_f \left[\cos \theta \frac{\partial(v_f \phi)}{\partial x} + \sin \theta \frac{\partial(v_f \phi)}{\partial z} \right] - \rho_s v_s \frac{\partial \phi}{\partial x} = 0, \quad (8)$$

$$\frac{\partial \bar{c}^i}{\partial t} + \rho_f \cos \theta \frac{\partial(v_f \phi c_f^i)}{\partial x} + \rho_f \sin \theta \frac{\partial(v_f \phi c_f^i)}{\partial z} + \rho_s v_s \frac{\partial}{\partial x} [(1 - \phi) c_s^i] = 0, \quad (9)$$

where \bar{c}^i is volatile mass per unit rock volume and can be converted to mass fraction via

$$c_{th}^i = \frac{\bar{c}^i}{\rho_f \phi + \rho_s (1 - \phi)}, \quad (10)$$

which is used as input for the thermodynamic module from the Tian et al. (2019) Part I (the subscript “th” indicates input variables for the thermodynamic module):

$$\left(\phi, c_s^{H_2O}, c_f^{H_2O}, c_s^{CO_2}, c_f^{CO_2} \right) = \Phi \left(P, T, \bar{c}_{th}^{H_2O}, \bar{c}_{th}^{CO_2} \right). \quad (11)$$

Equations (8)–(11) constitute the governing equations in this study.

The unknowns in the governing equations are the magnitude of fluid velocity (v_f), porosity (ϕ), bulk compositions (\bar{c}^i), and H_2O and CO_2 content in both phases (c_f^i, c_s^i)—eight unknowns in total. The thermodynamic equation (11) provides solutions to five unknowns, so it can be counted as five equations. Including equations (8) and (9), the total number of equations is eight, so the set of governing equations is closed. Note that the closedness of governing equations is premised on the prescription of flow angle (θ) and steady-state P - T structure of the slab. To be consistent with the steady-state P - T field, we solve the governing equations (8)–(11) until a steady state is reached (after ~ 6 Ma model time for a 5 cm/yr convergence rate).

The model yields the magnitude distribution of fluid velocity with predefined uniform flow direction by mass conservation, without resorting to the momentum conservation equation (i.e., Darcy's law). With the P - T path of a subducting slab predetermined, thermodynamics of local equilibrium dictates the amount of volatiles liberated from or absorbed to every rock parcel during each timestep of the model. Under steady state, with flow direction (θ) prescribed, mass conservation dictates that the magnitude of fluid flux is simply the integration of volatiles released or absorbed (i.e. the term $v_s(\partial \phi / \partial x)$ in equation (8) integrated along flow trajectories). Readers are referred to Appendix A for further details.

We note that avoiding the momentum conservation equation by prescribing the flow direction (θ) has positive and negative consequences. The downside is the lack of emergent, dynamic flows; instead, fluid flows are determined by choice of flow direction and conservation of mass along the selected flow paths. As briefly discussed in section 1, the upside is that the large uncertainties associated with the diversity of possible flow patterns yielded by various dynamic considerations is avoided. For example, two-phase dynamic model using viscous rheology suggests a high-permeability flow channel at the interface between slab and mantle wedge (Wilson et al., 2014), whereas those using viscoelastic rheology show the development of porosity waves within the slab (Morishige and van Keken, 2018). On smaller spatial scales (e.g., centimeter to meter), Plümper et al. (2017) and Malvoisin et al. (2015) show that flow channels and porosity waves can develop as well. Besides, viscoelastoplastic models suggest that faults formed during slab bending exert a strong control on the fluid flow directions and overall flow pattern within the slab (Faccenda et al., 2009). Indeed, there is various field evidence attesting to the complexity of fluid flows in subducting slabs (Ague, 2007; Barnicoat and Cartwright, 1995; Breeding et al., 2003, 2004; Galvez et al., 2013; Philippot and Selverstone, 1991; Piccoli et al., 2016; Putlitz et al., 2000). Designating flow direction (θ) as a free model parameter, however, enables

us to approximate the overall trend of fluid flows and explore it by setting θ to different values. Nevertheless, ignoring the flow dynamics does not revert the current model to the conventional open-system models. For example, the fraction of exsolved volatiles that is moved out and reacted upwards is determined ad hoc (Gorman et al., 2006), but this fraction is constrained by mass conservation in the current model such that porosity is maintained at a finite steady level.

In summary, the assumptions regarding the thermomechanical aspects of the slab in our model are as follows: (i) rigid plate with a prescribed subduction rate v_s ; (ii) constant densities for liquid (ρ_f) and solid (ρ_s) phases; (iii) steady-state P - T structure of the slab precalculated from canonical thermomechanical models. The assumptions in the reactive flow model are the following: (i) local equilibrium between liquid and solid phases; (ii) no diffusion or dispersion of H_2O and CO_2 ; (iii) flow direction θ is prescribed and uniform across the slab; and (iv) the reactive flow is solved until a steady state is reached.

3. Numerical Method

3.1. Initial and Boundary Conditions

We undertake timestepping for equations (8)–(11) to achieve the steady-state solution. The initial conditions are as follows: bulk volatile content \bar{c}_{th}^i are uniformly set to those of the incoming rocks on the left boundary; porosity (ϕ) and volatile content in both phases (c_f^i , c_s^i) are determined via the thermodynamic module (equation (11)); initial fluid speed (v_f) is zero across the modeled slab domain.

The incoming slab is assumed to be layered in lithology (Figure 1b) and thus has bulk volatile content: $\bar{c}_{th}^{CO_2} = 3.01$ wt% and $\bar{c}_{th}^{H_2O} = 7.29$ wt% (Plank and Langmuir, 1998) for a sedimentary layer from 0 to 0.5 km; $\bar{c}_{th}^{CO_2} = 2.95$ wt% and $\bar{c}_{th}^{H_2O} = 2.68$ wt% (Kerrick and Connolly, 2001b) for a MORB layer from 0.5 to 2.5 km; $\bar{c}_{th}^{CO_2} = 2.84$ wt% and $\bar{c}_{th}^{H_2O} = 2.58$ wt% for a gabbroic layer from 2.5 to 6.5 km; and $\bar{c}_{th}^{CO_2} = 0.02$ wt% and $\bar{c}_{th}^{H_2O} = 1$ wt% (Hart and Zindler, 1986) for a slab mantle layer from 6.5 to 8 km. Note that 1 wt% H_2O content in serpentinized peridotite roughly corresponds to a serpentinization degree of $\sim 8\%$ (Carlson and Miller, 2003). The H_2O and CO_2 content in the altered gabbro is adopted from typical metabasalt values (Kerrick and Connolly, 2001b), and renormalized using the nonvolatile composition for gabbro in Hacker (2008). This very likely represents an upper limit because hydrothermal alteration decreases with depth (Kelemen and Manning, 2015). In fact, gabbros altered in mid-ocean ridges are estimated to contain 0.2–1.3 wt% H_2O (Carlson, 2003; Hacker et al., 2003), but all these estimates exclude the contribution from volatile addition in the outer rise near subduction (Peacock, 2001). If hydrothermal changes at both mid-ocean ridges and outer rises are taken into account, the high gabbro volatile content adopted here could represent an upper limit.

As for boundary conditions, since the governing equation for flow speed (v_f) is first order in space, only one boundary condition along the flow paths is needed. For flow paths originating from the slab base, no-flux ($v_f = 0$) boundary condition is prescribed (Figure 1b). However, for the ghost points above the upper boundary in the numerical grid, Neumann boundary conditions $\partial v_f / \partial z$ and $\partial \bar{c}_{th}^i / \partial z$ are adopted for flow speed and bulk volatile content. The left and right boundary conditions depend on flow direction (θ). When $\theta \leq 90^\circ$, the flow paths originate from the left and basal boundaries, so we let $v_f = 0$ and $\bar{c}_{th}^i = \bar{c}_{th}^i|_{incoming}$ on the left, and $\partial v_f / \partial x = 0$ and $\partial \bar{c}_{th}^i / \partial x = 0$ on the right. When $\theta > 90^\circ$, the flow paths originate from the right and basal boundaries, so we let $\partial v_f / \partial x = 0$ and $\bar{c}_{th}^i = \bar{c}_{th}^i|_{incoming}$ on the left, and $v_f = 0$ and $\partial \bar{c}_{th}^i / \partial x = 0$ on the right.

3.2. Solution Procedure

The nonlinear character of the governing equations (8)–(11) is evident by inspection. For example, equation (10) shows that bulk volatile content depends on fluid flow (v_f , θ), porosity (ϕ), and volatile content in each phase (c_f^i , c_s^i), among which porosity and phase volatile content depend further on bulk compositions through thermodynamics expressed in equation (11). To solve this equation set, we employ PETSc (Portable, Extensible Toolkit for Scientific computing, Balay et al., 2018), following the procedure illustrated in Katz et al. (2007) to write down the residuals of governing equations (8) and (9). The solution of every timestep is handled by the nonlinear solver provided by PETSc, and the special treatment in our solution procedure is that we emplace the thermodynamic module (equation (11)) within every evaluation of residuals at each Newton iteration.

At the sites where devolatilization onsets, there will be pulses of volatile production owing to the increase of porosity from ideally zero to some finite value determined by thermodynamics. These pulses of volatile

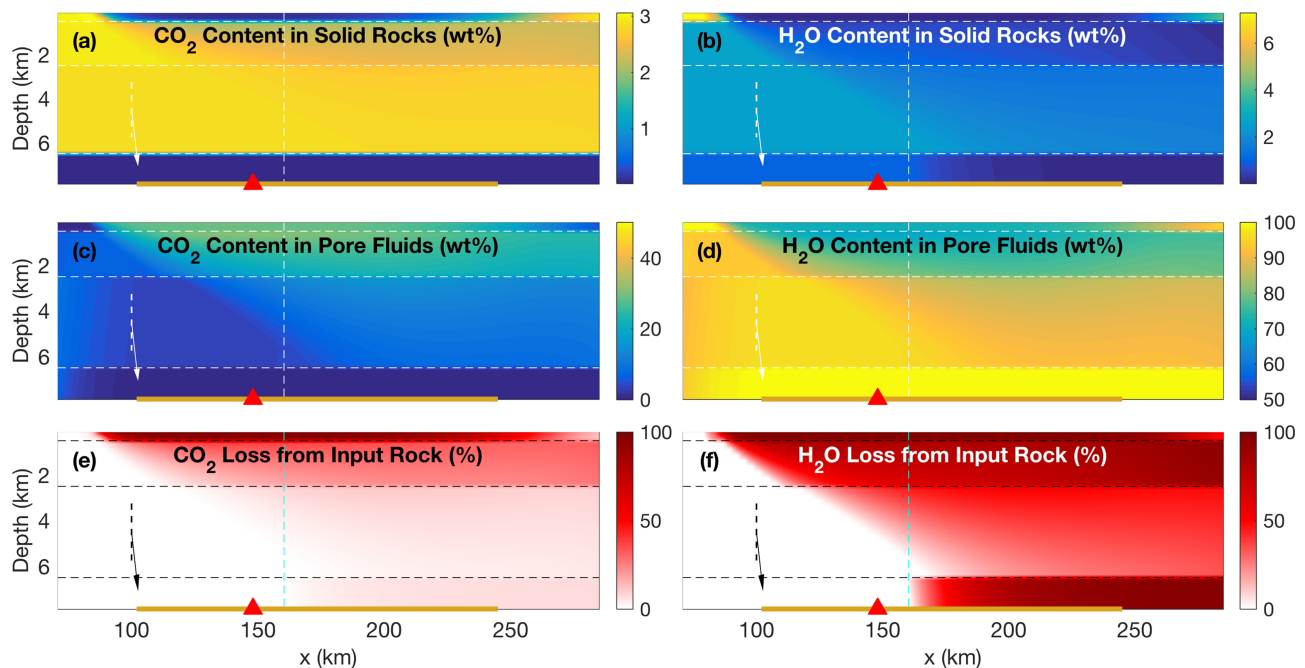


Figure 3. Results for the closed-system model. Left panels (a, c and e) are for results on CO_2 , and right panels (b, d and f) are for H_2O . Horizontal dashed lines (white or black) mark the lithological interfaces, and long vertical dashed lines mark the position where the basal serpentinized upper mantle starts to devolatilize. Divergent colormaps (blue-white-red) are used for panels (e) and (f) where red color corresponds to positive values (volatile loss) and blue color corresponds to negative values (volatile gain). Volatile loss (or gain) in (e) and (f) is calculated relative to its content on the left boundary. Succeeding figures adopt the same line, arrow and color conventions. The brown line and red triangle at the base of each panel have the same meaning as in Figure 2, but are placed at the panel base to avoid cluttering the display of the top sedimentary layer.

production along the envelope of the devolatilizing region eventually contribute to integrated volatile fluxes and cause small fluctuations in the computed fluxes. To focus on the general trend and overall pattern of volatile fluxes within and atop the slab, the results returned by the solution procedure above are postprocessed through a smoothing step. Different length scales of smoothing have been experimented with and we choose 12 numerical grid points (corresponding to 3 km) as the spatial span for smoothing. Details on the smoothing are provided in Appendix A.

4. Results

Before presenting the results for the open-system reference model, we first provide the closed-system results (Figure 3) with a twofold goal: first, to compare our closed-system results with the previous, purely thermodynamic model that assumes a closed system and second, for later comparison with the open-system reference model to elucidate the open-system effects.

4.1. Closed System

The closed system is characterized by the fact that there are no mass fluxes into or out of the rocks of interest, leaving the bulk compositions unaltered. As a result, the bulk CO_2 and H_2O content of the incoming rocks stay unchanged as subduction proceeds with a speed v_s ; that is, these bulk values in the slab remain equal to those at the inflow boundary (left side in Figure 1b). Such a closed-system model corresponds to that typically used in earlier studies, where a representative but fixed bulk composition is used for each rock type to construct thermodynamic phase diagrams over which various subduction geotherms are superimposed (Hacker, 2008; Hacker et al., 2003; Peacock, 1990, 1991; van Keken et al., 2011).

With the P - T field of a hot slab (Figure 2), Figure 3 shows our closed-system results. Left panels are results on CO_2 , and right panels on H_2O . From top to bottom, the rows of the panels show CO_2 and H_2O content in the solid rock phase, liquid volatile phase, and their loss relative to the starting values on the inputting boundary. Of course in a closed system, there should be no volatile loss. However, in closed-system devolatilization models it is conventionally assumed that volatiles, once exsolved, are immediately extracted from the bulk

system (without altering the bulk composition) (Peacock, 1990, 1991; Hacker, 2008; Hacker et al., 2003; van Keken et al., 2011). In this context, a general trend of CO₂ and H₂O loss from rocks can be seen with along-slab distance in Figures 3a and 3b, and more clearly in Figures 3e and 3f. However, there is a reversal of this trend near the slab distance ~210 km in the top sedimentary layer (e.g., Figure 3a). It can also be seen from Figures 3c and 3d that, within each lithological layer, the coexisting liquid phase is gradually more CO₂-rich as subduction goes deeper, except where the trend reversal takes place.

Under the model assumption regarding extraction from a closed system, the volatile loss in Figures 3e and 3f is the change in volatile content of the solid phase from its initial value. Since the amount of liquid phase in equilibrium depends on *P-T* conditions, the nonuniform *P-T* field within the slab yields varying extent of volatile loss in the closed-system model. The trend reversal in Figure 3 can be understood by superimposing the top-layer geotherms over the phase diagram for closed systems (van Keken et al., 2011). The *P-T* conditions in the segment beyond ~210 km in the top layer exceed the *P-T* curve for the onset of devolatilization, but to a lesser extent than the *P-T* conditions in the segment before ~210 km, leading to a smaller degree of devolatilization. Similar trend reversal of closed-system volatile loss can also be observed for the warm subduction geotherm in Kerrick and Connolly (2001a).

Depths of volcanic arcs to slab surface range from ~70 to ~170 km (Syracuse and Abers, 2006), which correspond to along-slab distances of ~100 to ~250 km in Figure 3. Closed-system model predictions, shown in Figures 3a, 3b, 3e, and 3f, indicate that slab sediments almost completely lose CO₂ & H₂O at forearc depths; the basaltic and gabbroic layers can supply significant H₂O but only limited CO₂ at subarc depths; the slab mantle lithosphere can release almost all of its H₂O at subarc depths. All these results are consistent with the previous studies that assume closed systems and consider hot subduction geotherms (Kerrick and Connolly, 1998; Kerrick and Connolly, 2001a; Kerrick and Connolly, 2001b).

To facilitate later comparison, it is worth noting the implications of the closed-system model for the open-system behaviors in the succeeding sections. First, the basal slab mantle layer in this model contains negligible CO₂ and serves essentially as a water supplier. Because hydrated slab mantle has only a small set of hydrous minerals (i.e., talc, brucite, serpentine, chlorite), H₂O loss in this layer is more abrupt and complete relative to in basaltic and sedimentary layers. A sudden onset of the supply of the basal H₂O will, in later sections on open-system flow, lead to significant H₂O infiltration. Second, at the peridotite-gabbro and gabbro-basalt interfaces (6.5 and 2.5 km deep into the slab, respectively), there is a sharp CO₂ concentration gradient in the liquid phase (Figures 3c and 3d). Fluid ascent in the open systems would inevitably cause H₂O-rich and CO₂-poor fluid infiltration that enhances decarbonation (Gorman et al., 2006). Third, the CO₂ concentration in the liquid phase decreases from the basaltic to the sedimentary layer, suggesting the potential for carbonation by fluid flow down the gradient of CO₂ concentration.

4.2. Open-System Reference Model

Taking all the parameters for the closed-system model above, the reference model additionally considers fluid flows with a uniform direction $\theta = 90^\circ$ (Figure 1b), namely, fluid flow is normal to the direction of slab motion (v_s). The results of the steady-state solution to this open-system model are presented in Figure 4. The panel layout of Figure 4 is the same as that of Figure 3 except for the three additional panels in the bottom two rows. These show the porosity (Figure 4g and 4i) and volatile flux (Figure 4h) distribution within the slab. To elucidate and further highlight the open-system effects, Figure 5 maps the differences in CO₂ and H₂O loss (or gain) between the closed- and open-system models, that is, volatile loss in the open system minus that in the closed system. We next consider the reference model results in each layer of the slab, from bottom to top.

The basal slab mantle layer does not experience fluid infiltration because the flows are upward and there is no flux at the bottom boundary. Figure 4c and 4d shows that the devolatilized liquid phase is almost pure H₂O, given that the inputting peridotitic rock contains negligible bulk CO₂ (0.02 wt%). The H₂O loss is thus abrupt and complete (Figure 4f), similar to that for the closed-system model.

On top of the base layer, the gabbro layer is fluxed by nearly pure H₂O sourced from below (Figure 4c and 4d). As a result, the infiltration and fractionation effects discussed in Part I come into play. The very H₂O-rich and CO₂-poor fluids will infiltrate the base of the gabbro layer, causing enhanced decarbonation and inhibited dehydration. The enhanced CO₂ loss is evident in Figure 5a, but the expected reduction in H₂O loss is not as clear in Figure 5b. This can be explained by the fractionation effect detailed in Part I. Because

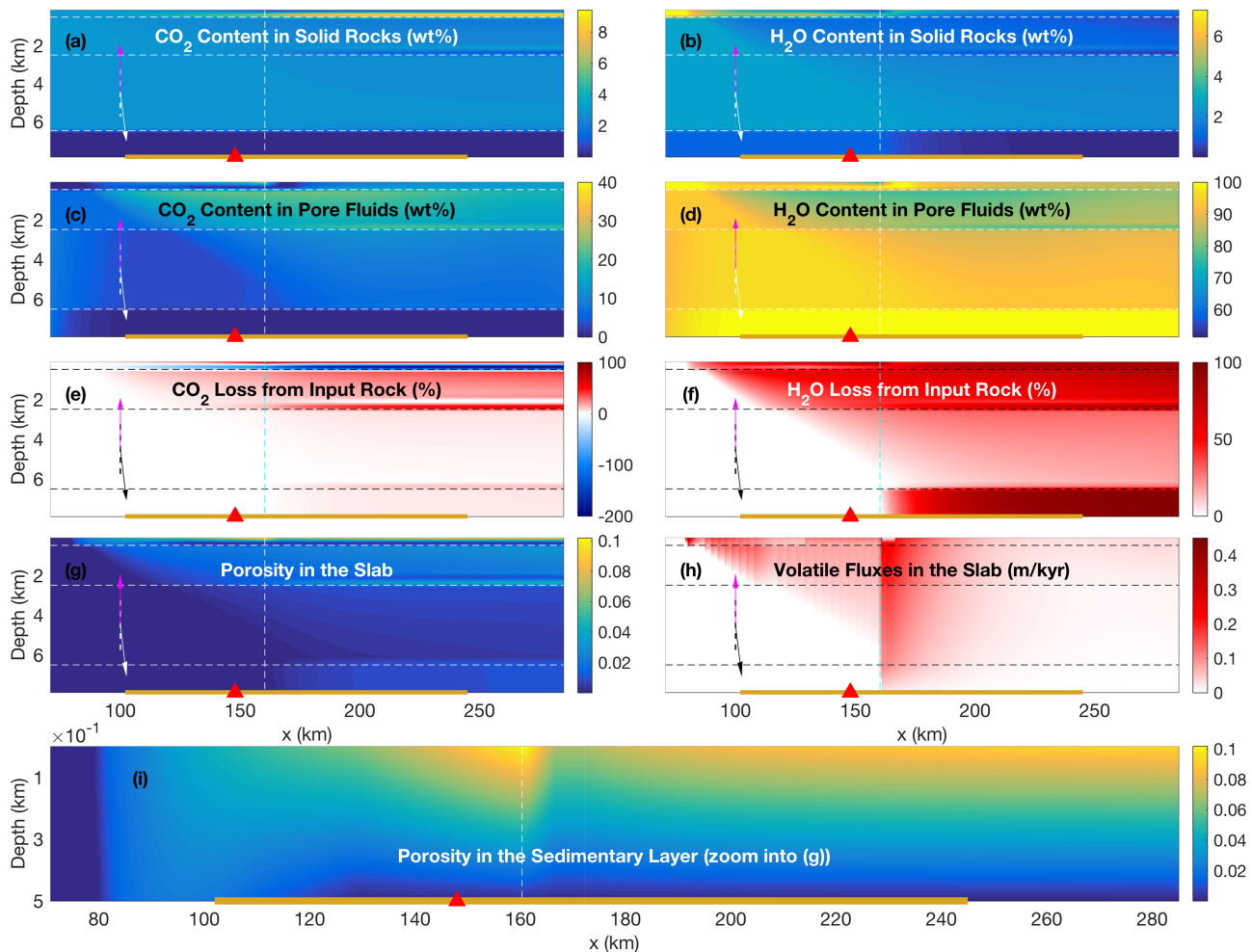


Figure 4. Results for the open-system reference model. Left panels (a, c, e and g) are for results on CO_2 , and right panels (b, d, f and h) are for H_2O . The magenta arrows denote the direction of fluid flow (90° in the reference model) relative to slab extension, whereas the black or white arrows denote the direction of gravity. The short dashed lines (white or black) are a reference direction normal to the slab extension. Red color in the divergent colormap for volatile flux (panel h) means upward fluid flow, whereas blue color means downward flow. Note the different horizontal and vertical scales in the plots, and the true angle between gravity and the flow direction should be 145° . Panel (i) maps the porosity distribution only for the top sedimentary layer in panel (g).

increased decarbonation reduces the ratio of CO_2 over H_2O in the bulk system of solid plus liquid, the onset temperature of devolatilization decreases at the base of the gabbro layer. Given that temperatures within the modeled slab are held fixed, such a decrease in the onset temperature means devolatilization of the bulk system becomes easier, so the resultant increase of devolatilization extent can offset the inhibitive effect on H_2O loss induced by the infiltration. The elevated extent of devolatilization is also reflected by the higher porosity at the base of the gabbro layer in Figure 4g.

The infiltration effect is strongest at the peridotite-gabbro interface because the concentration gradients of CO_2 and H_2O in the liquid phase are the steepest (Figure 4c and 4d). Above the interface, the liquid phase compositions have been adjusted by the buffering reactions drastically occurring at the interface, so the infiltration effect weakens. In consequence, the bulk interior of the gabbro layer is dominated by the fractionation effect. At and after the onset of devolatilization, preferential H_2O loss causes increased difficulty in devolatilization and thus inhibits overall volatile loss in the bulk interior (Figure 5).

Further up, the H_2O -rich and CO_2 -poor fluids (Figures 4c and 4d) derived from the gabbro layer infiltrate the base of the basalt layer, similar to the scenario at the base of gabbro layer. Likewise, relative to the closed system, enhanced CO_2 loss and approximately unmodified H_2O loss take place at the layer base (Figure 5), and the overall CO_2 and H_2O loss is inhibited in the layer interior. The porosity elevation immediately above the gabbro-basalt interface is even more discernible in this case (Figure 4g). Moreover, elevated porosity

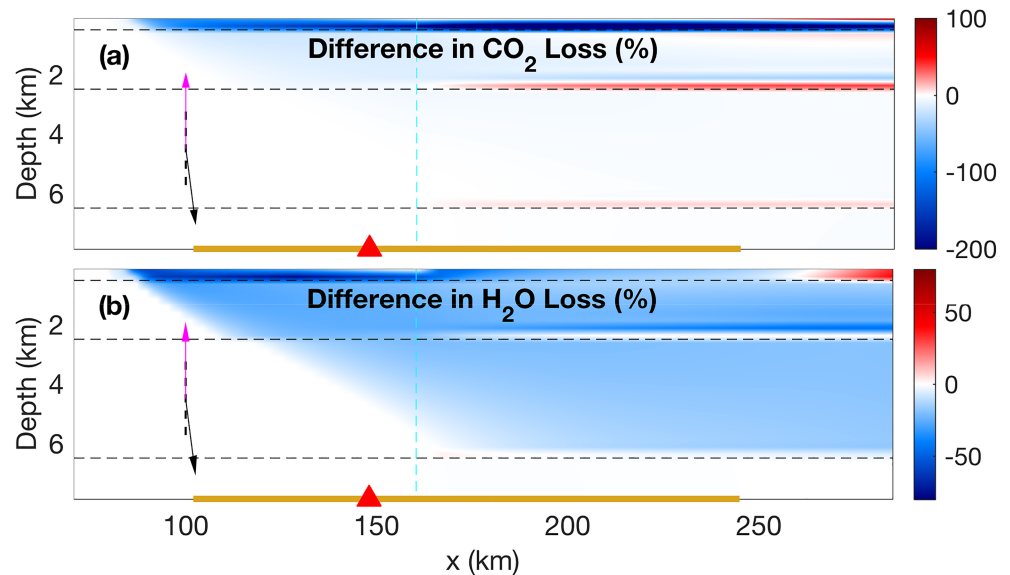


Figure 5. Differences in (a) CO_2 and (b) H_2O loss (or gain) between the open- and closed-system models. The difference is calculated by rock CO_2 or H_2O loss in the open system minus that in the closed system, and percentage values are relative to the initial rock volatile content. Note that, unlike in Figures 3 and 4, red color means enhanced loss or diminished gain, whereas blue color means diminished loss or enhanced gain.

levels reflect higher extent of devolatilization. According to our parameterization in the Tian et al. (2019) Part I, higher extent of devolatilization corresponds to higher CO_2 and lower H_2O concentrations in the coexisting liquid phase, which are also evident at ~ 2.5 km depth in Figures 4c and 4d. Upward infiltration of these fluids, coupled with the fractionation effect, gives rise to the diminished volatile loss immediately above the region of enhanced decarbonation (blue stripes ~ 2 km deep in Figure 5). Note also that in Figure 5 the degree of decarbonation is higher at the basalt base than at the gabbro base, which is consistent with the higher integrated fluid fluxes at the shallow lithological interface (Figure 4h).

Figures 4c and 4d show that the fluid infiltration at the base of the topmost sedimentary layer is down the CO_2 and up the H_2O concentration gradients. As is inferred from the closed-system model, the infiltration will result in carbonation reactions in the sediments immediately above the lithological contact, which is demonstrated by the negative values of CO_2 loss (i.e., CO_2 gain by the sediments) in Figure 4e. Figure 5a compares the CO_2 loss between the open- and closed-system models; carbon sequestration in the top sedimentary layer is more evident. In Figure 5b, it can be seen that H_2O loss in the sedimentary layer diminishes before ~ 250 km along the slab coordinate. This is due to the fractionation effect discussed in Part I: carbonation increases the ratio of bulk CO_2 over H_2O , which further raises the onset temperature of devolatilization and in turn inhibits dehydration. As for the enhanced H_2O loss after ~ 250 km in Figure 5b, it actually stems from the reversal of trend in the H_2O loss calculated for the closed-system model (e.g., Figure 3f).

A common feature above the gabbro–basalt and basalt–sediment interfaces in Figure 5a is the formation of paired stripes in red and blue, but the vertically reversed color order for the stripe pair in the sedimentary layer indicates that decarbonation follows carbonation along infiltration. This is because the former stripe pair is caused by infiltration down a CO_2 gradient, whereas the latter is by that up the gradient. Another noteworthy feature in Figure 5 is that the starting positions of the infiltration-induced stripes in the basalt and gabbro layers coincide horizontally with the onset of dehydration of the slab upper mantle. This coincidence reflects the potential for fluids from hydrated lithospheric mantle to remobilize slab H_2O and CO_2 . In fact, the enhanced infiltration into the top sedimentary layer causes considerable carbonation that substantially reduces the porosities and fluid fluxes immediately after ~ 160 km along the slab (Figures 4g–4i).

Close examination of Figure 4h suggests that the volatile fluxes fluctuate laterally before the onset of slab mantle dehydration at ~ 160 km. This is because the onset of devolatilization at different slab depths occurs at different horizontal positions that are laterally separated from one another. Since the onset of devolatilization corresponds to a pulse of volatile production, after being vertically integrated into volatile fluxes, these pulses cause lateral fluctuation in volatile flux distribution. Appendix A discusses this issue further.

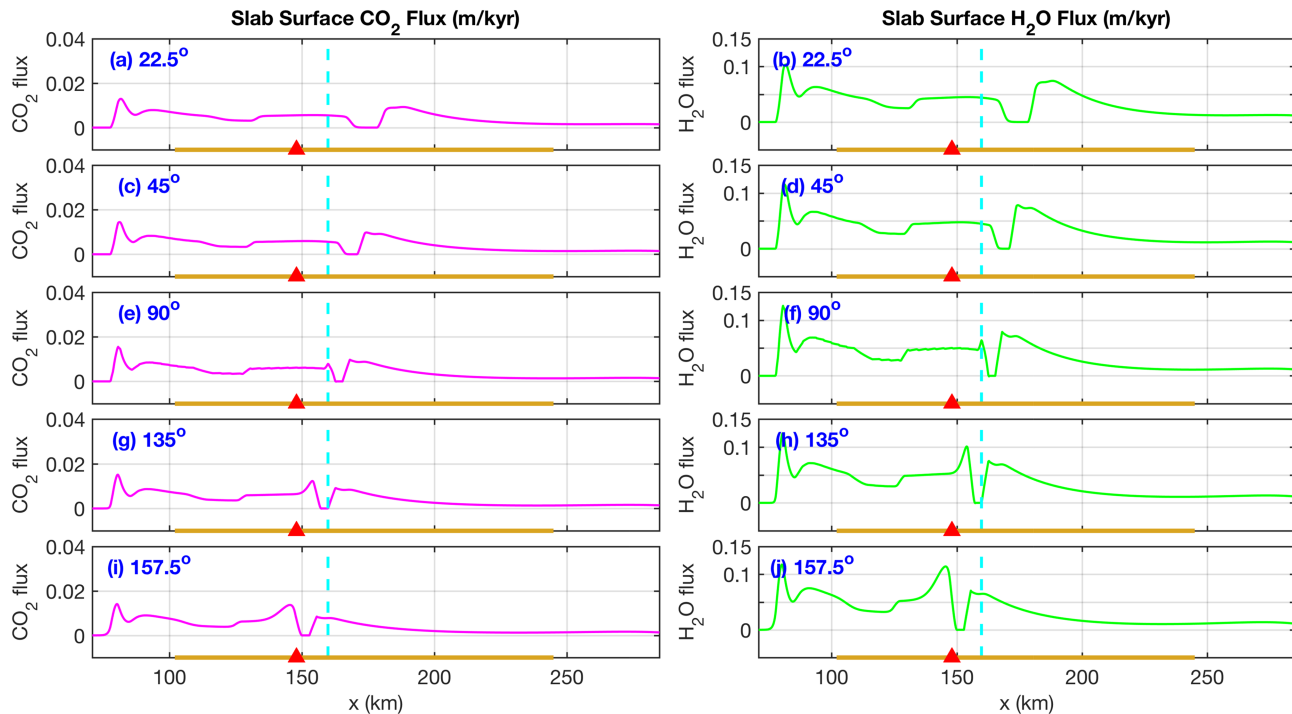


Figure 6. CO₂ (left panels: a, c, e, g and i) and H₂O (right panels: b, d, f, h and j) fluxes along the slab surface as a function of fluid flow direction (θ). Note that the panels (e and f) in the middle row are the fluxes from the reference model in section 4.2. Cyan dashed lines mark the starting position of slab mantle devolatilization and this convention applies in the succeeding figures.

4.3. Effect of Flow Direction

Different flow trajectories pass through areas with different P - T conditions that are associated with different volatile partition coefficients. Hence, volatile loss and gain during reactive flow are path dependent, and we assess the impact of fluid flow direction (θ) on CO₂ and H₂O fluxes emanating from slab surface. Figure 6 shows the slab surface CO₂ (left panels) and H₂O (right panels) fluxes with flow angles of 22.5°, 45°, 90°, 135°, and 157.5°. The case of flow angle $\theta = 90^\circ$ is the open-system reference model already presented in section 4.2. Other than flow angle, all the parameters for model runs in Figure 6 are identical to those in the reference model. The flow angles 22.5°, 45°, 90°, 135°, and 157.5° are chosen to spread between 0° and 180°, and thus representative of various flow scenarios; other choices of flow angles do not affect our conclusion. We also note that the angle of 22.5° corresponds to downward flow, which could occasionally occur in localized settings (Faccenda et al., 2009). The consideration of this flow scenario is primarily to explore as completely as possible the spectrum of within-slab flow patterns.

Figure 6 shows profiles of the slab surface volatile flux (i.e., $[v_f \phi c_f^i]_{z=0} \sin \theta$). All the profiles have a peak near ~80 km along the slab, caused by the devolatilization of the top sedimentary layer. In addition, there is a dip in all the flux profiles around the starting position of slab mantle devolatilization (~160 km). This sharp drop of surface flux stems from the boost of carbonation reactions by slab mantle devolatilization, which reduces the top-layer porosity (ϕ) and further the surface flux ($v_f \phi$). The shift in position of this dip is due to the change of flow direction that advances ($\theta > 90^\circ$) or retreats ($\theta < 90^\circ$) the carbonation reaction in the top sedimentary layer. A more striking feature in Figure 6 is a second flux peak that emerges at the average position of global arcs projected onto the slab surface (red triangle). As shown in Figures 6g–6j, this peak appears only when flow angle $\theta > 90^\circ$, that is, for fluid flows that are nearly slab-parallel and up-dip. If it is further assumed that magmas generated by flux melting traverse the mantle wedge vertically without deflection (Grove et al., 2012), Figure 6 implies that up-slab fluid flow is responsible for the magma supply to volcanic arcs.

The emergence of the subarc flux peak in Figure 6 can be explained by Figure 7, which maps the difference in fluxes ($v_f \phi$) between models with flow angle $\theta \neq 90^\circ$ and the reference model with $\theta = 90^\circ$. The flux increase in Figure 7 can be understood by inspecting equation (A2): fluid fluxes accumulate along flow paths

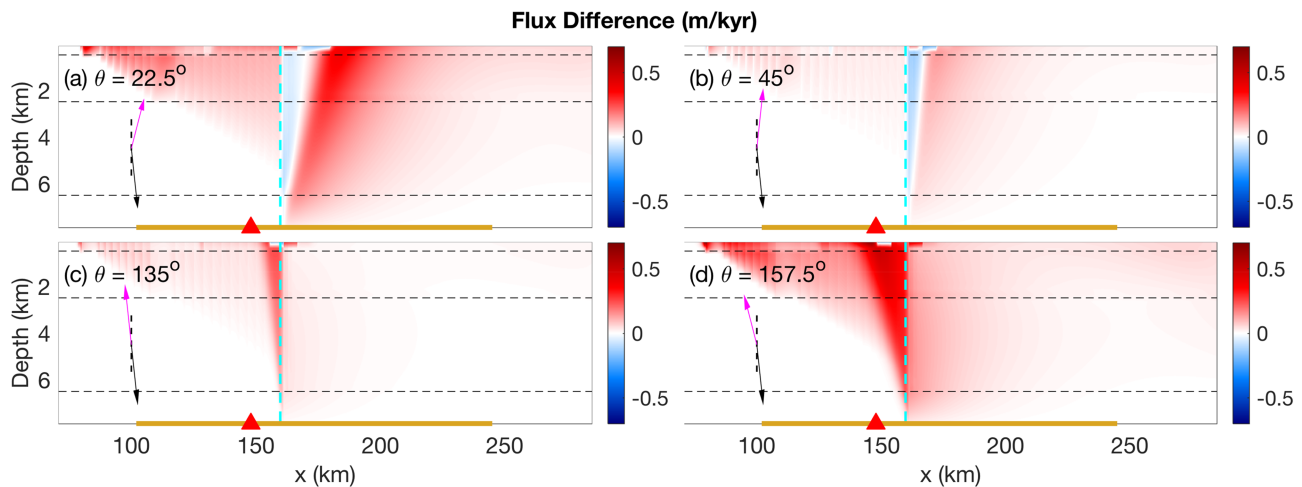


Figure 7. The difference in fluid fluxes ($v_f \phi$) between the models with flow angle $\theta \neq 90^\circ$ and the open-system reference model with $\theta = 90^\circ$. Red color corresponds to flux increase, and blue color to flux decrease, both relative to the reference model results. Arrows and dashed lines bear the same meaning as in preceding figures. Note that the small patches in the sedimentary layer around ~ 160 km is related to the sharp porosity reduction due to strong carbonation, read the reference model section 4.2 for more details. (a) $\theta = 22.5^\circ$; (b) $\theta = 45^\circ$; (c) $\theta = 135^\circ$; (d) $\theta = 157.5^\circ$.

and longer paths tend to cause larger fluxes. Moreover, when $\theta > 90^\circ$, additional flux increase is caused by flow trajectories tapping into the region of slab mantle devolatilization (Figures 7c and 7d). Conversely, when $\theta < 90^\circ$, the flux diminution in Figures 7a and 7b is caused by flow trajectories passing through regions before the onset of slab mantle devolatilization. As flows with $\theta > 90^\circ$ can transport more volatiles to slab surface, this explains the emergence of flux peak near ~ 150 km in the flux profiles in Figures 6g–6j.

4.4. Effect of Slab Age

Published closed-system and 1-D open-system studies (Gorman et al., 2006; Hacker, 2008; Kerrick and Connolly, 1998, 2001a, 2001b; van Keken et al., 2011) show that high-temperature subduction geotherms promote slab devolatilization and thus increase slab surface volatile fluxes. We test this hypothesis using our 2-D open-system model. Results with flow angle $\theta = 90^\circ$ and slab ages ranging from 10 to 60 Ma are shown in Figure 8, where it can be seen that, for old slabs with cold geotherms, devolatilization is deferred to greater depths. For the coldest slab (60 Ma old) in this study, there is almost no dehydration or decarbonation in the range of subarc depths. In general, relative to the 10 Ma slab in the reference model, old, cold slabs will release less volatiles around subarc depths, therefore promoting CO_2 & H_2O recycling into deep mantle (Rüpke et al., 2004).

Flow angles in Figure 8 are all 90° and, according to our assessment of the directional effect of flows, it can be inferred that up-slab flows ($\theta > 90^\circ$) will produce flux peaks. However, the positions of these peaks are controlled by the position of the onset of slab mantle devolatilization. Given that the onset of slab mantle devolatilization is also deferred to greater depths in old slabs (Figure 8), up-slab flows would not affect the subduction efficiency of H_2O and CO_2 (see section 4.7). In other words, cold slabs promote H_2O and CO_2 recycling even if within-slab flows are upward along the slab.

4.5. Effect of Serpentinization

It is commonly proposed that hydration of slab lithospheric mantle takes place in fast-spreading oceans at the outer rise near the trench (Ranero et al., 2003); subsequent dehydration leads to slab embrittlement, which has been invoked for interpreting subduction zone seismicity (Kerrick, 2002; Peacock, 2001; Paulatto et al., 2017; Seno and Yamanaka, 1996). Observational seismic studies infer the extent of serpentinization to be 5–31% (Garth and Rietbrock, 2014; Garth and Rietbrock, 2017; Grevemeyer et al., 2007), which corresponds to H_2O content of 0.6–3.5 wt% for hydrated slab mantle. Given this uncertainty of H_2O content and its control on the within-slab flux pattern (e.g., Figure 7), we test how this factor affects slab volatile storage and surface fluxes by varying the H_2O content in the incoming slab mantle lithosphere from 0.5 wt% ($\sim 4\%$ serpentinization) to 10 wt% ($\sim 76\%$ serpentinization). Panels in Figure 9 show the resultant variation of CO_2 and H_2O fluxes along the slab surface, where 1 wt% H_2O is the value used for the reference model. First, the position of onset for lithosphere devolatilization moves from depth of ~ 125 to ~ 80 km as the hydration extent

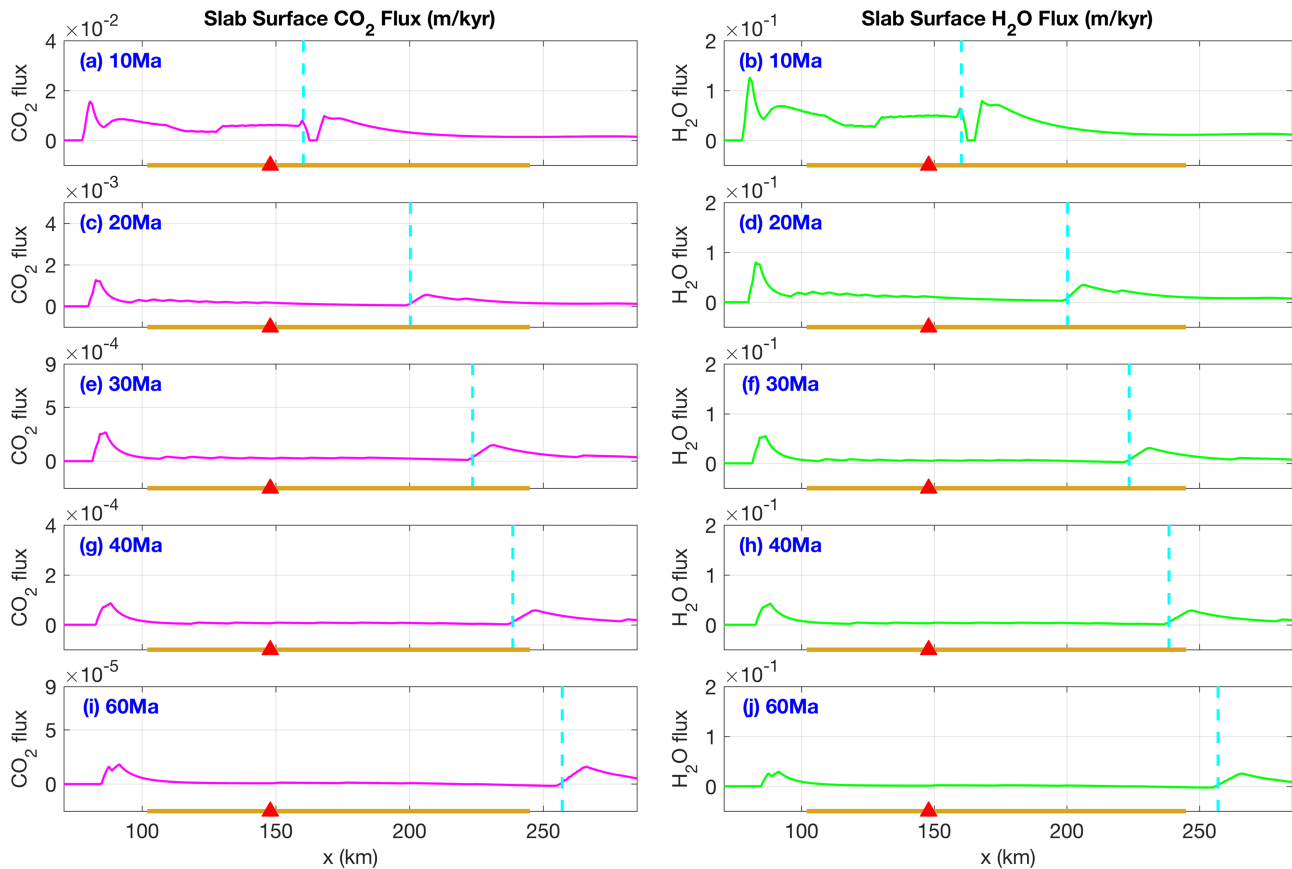


Figure 8. CO₂ (left panels: a, c, e, g and i) and H₂O (right panels: b, d, f, h and j) fluxes along the surfaces of slabs with different ages. The result from the reference model with a 10 Ma slab is also plotted in the top row for comparison. Note the shift of the position for the onset of slab mantle devolatilization and the flux peak associated with it. Also note that the y-axis scales decrease from top row to bottom for CO₂ fluxes.

of incoming slab increases. This is because increasing the bulk H₂O content while keeping bulk CO₂ constant (negligibly small 0.02 wt%) decreases the onset temperature of devolatilization. Second, the magnitudes of slab surface fluxes are substantially increased by the elevated basal H₂O content. Figures 9e–9h show that serpentinite dehydration can dominate other controls of slab surface CO₂ and H₂O fluxes and thus can play a crucial role in arc magmatism and subduction-zone volatile recycling (Shimoda and Kogiso, 2019).

In Figure 10, the differences in CO₂ and H₂O loss relative to that of the reference model are mapped for different hydration states of the slab mantle. For the smaller extent of hydration (Figures 10a and 10b), the weakened infiltration leads to general reduction in reaction progress, as demonstrated by the decrease in both the CO₂ gain at the sites of carbonation (red stripes in Figure 10a), and the CO₂ loss at the sites of decarbonation (blue stripe/regions in Figure 10a). In particular, there is a stripe pair above the basalt–gabbro interface in Figure 10a, but vertically in reverse order to that in Figure 5a. This is still attributable to the diminished infiltration flux as explained above. By contrast, for higher extent of slab mantle hydration (Figures 10c–10f), stripe pairs similar to those in Figure 5a also appear in Figures 10b and 10e, but are pushed to upper levels due to the increased infiltration flux. Moreover, for very strong infiltration as in Figure 10e, decarbonation is so strong that even the carbonation within the basalt layer is offset (white stripe at ~2 km in Figure 10e). If inspected closely, a red-blue stripe pair appears at the peridotite–gabbro interface at ~6.5 km in Figure 10e, which is not the case for the reference model in Figure 5a, and the reason is simply that the stronger infiltration makes the stripe pair discernible.

Quantitatively, for the intensively infiltrated basalt layer in Figures 10c and 10e, CO₂ loss can be enhanced to as high as 100%, whereas for the even more intensively infiltrated sedimentary layer, the rise in CO₂ gain can be as high as 300%. In other words, enhanced infiltration extracts an extra amount of CO₂ from the gabbro and basalt layers along flow pathways, but much of the extracted CO₂ is merely redistributed into

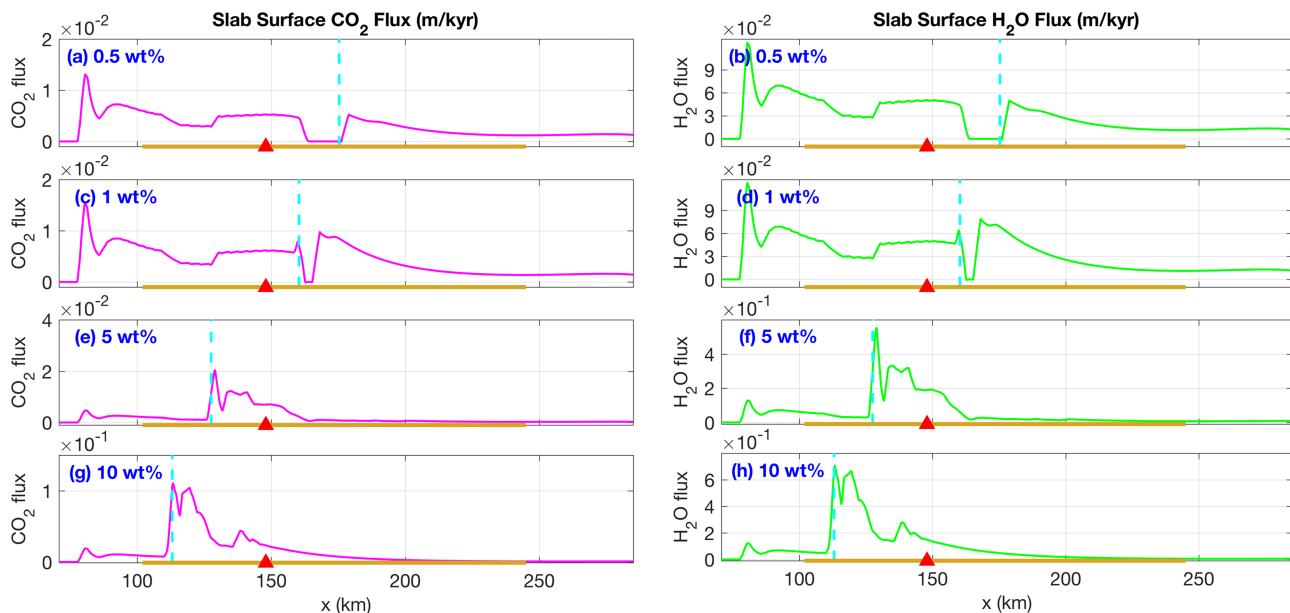


Figure 9. Slab surface CO_2 (left panels: a, c, e, and g) and H_2O (right panels: b, d, f, and h) fluxes as a function of initial H_2O content in the basal layer. The reference model (section 4.2) contains 1 wt% H_2O and its results are plotted in panels (c) and (d) for comparison. The cyan dashed lines mark the onset of dehydration of this basal layer. Note the increase of y-axis scales in the lower panels.

the top sedimentary layer. By comparing Figures 9c and 9e, or Figures 9c and 9g, it can be inferred that not all of the infiltration-induced CO_2 transfer is deposited in the sedimentary layer, a fraction of it escapes the slab top and contributes to the surface flux increase.

H_2O loss or gain differs from that of CO_2 . For the basalt and gabbro layers, both are infiltrated by H_2O -rich fluids that cause decarbonation above the layer contacts. As illustrated in the Tian et al. (2019) Part I, fractionation caused by decarbonation leads to a larger extent of overall devolatilization. The enhanced H_2O loss at depths ~ 2.5 and ~ 6.5 km in Figures 10d and 10f is a result of this. For the top sedimentary layer, however, it is infiltrated by flow down a CO_2 concentration gradient, so the fractionation caused by carbonation leads to inhibited H_2O loss, as reflected in Figure 10d. Different from that in Figure 10d, the top sedimentary layer in Figure 10f experiences more H_2O loss. This is because the stronger infiltration down the CO_2 gradient also induces dehydration that counteracts the fractionation effect that is dominant for the case in Figure 10d.

It is worth noting that field studies document the occurrence of a metasedimentary layer immediately on top of serpentinized slab mantle, where the sediments first experience decarbonation/hydration and second carbonation/partial dehydration (Brovarone and Beyssac, 2014; Piccoli et al., 2016). The flow in the outcrops are inferred to be confined into up-slab fluid channels. This field-documented two-stage flow event can be roughly elucidated by the current model. Taking Figure 10e for illustration, if there are channels tapping fluids from dehydrating mantle lithosphere in an up-slab direction (e.g., Figure 7d), then the subducting sediments will be infiltrated by very H_2O -rich fluids, leading to the first stage decarbonation/hydration. At greater depths, when the tapped fluids scavenge CO_2 by passing through gabbro and basalt layers, carbonation reaction can take place in the sedimentary layer, accounting for the second-stage flow documented in the field.

4.6. Effect of Sediment Removal

For all of our models so far, a sedimentary layer of 500 m is assumed to cover the slab top and not detach during subduction. However, the sediments are subject to off-scraping in the accretionary prism of subduction zones (Raymond, 2019). In addition, the slab surface sediments that survive off-scraping at trenches are further subject to removal by diapirism. Previous studies (Behn et al., 2011; Marschall and Schumacher, 2012) showed that a sedimentary layer >100 m thick and $\sim 200 \text{ kg/m}^3$ lighter than surrounding peridotites may form rising diapirs that traverse the mantle wedge. Kelemen and Manning (2015) propose that diapirs entraining carbonates are an important avenue for carbon release to mantle lithosphere. We therefore assess

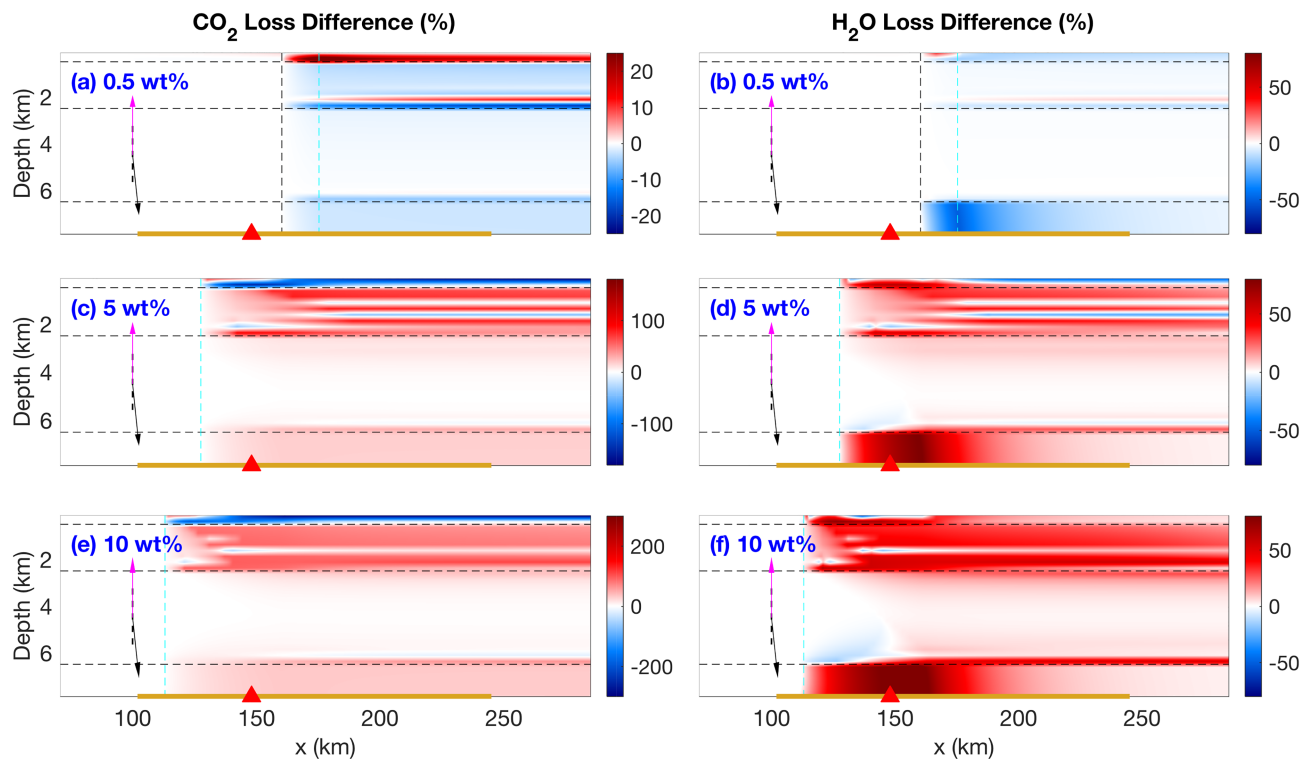


Figure 10. Differences in CO_2 (left panels: a, c, and e) and H_2O (right panels: b, d, and f) loss relative to the reference model, caused by various initial H_2O content in the slab mantle. The percentage values are relative to the initial rock volatile content, as in Figure 5. Red color corresponds to enhanced volatile loss or diminished volatile gain, whereas blue color corresponds to diminished loss or enhanced gain. Note that the thin vertical black dashed lines in (a) and (b) mark the onset of dehydration in hydrated slab mantle for the reference model and are plotted here for better comparison.

the impact of sediment removal on slab volatile storage and emission based on a simplified model setup: (i) the topmost 500-m-thick sedimentary layer in the reference model is replaced by basalt of the same composition as the underlying layer, mimicking the scenario of complete removal of sediments; (ii) this replacement basaltic layer is excluded during calculations of the resultant volatile fluxes and subduction efficiency (see next section). (iii) fluid flow angles are varied among 22.5° , 45° , 90° , 135° , and 157.5° to examine the resultant slab surface fluxes.

For this three-layer model with a 90° flow angle, Figure 11 maps the volatile loss within the slab. Regarding CO_2 loss (Figure 11a), except for the thin sheet of CO_2 gain above the basalt-gabbro interface, the entire plate loses CO_2 , and the loss can reach a maximum of $\sim 70\%$ at the infiltration site from gabbro to basalt. The thin sliver of up to 25% CO_2 gain is due to the infiltration-related carbonation, as previously explained. In contrast, H_2O loss in Figure 11b is similar to that of the reference model. This is because the sedimentary layer, even if it survives the removal, should dehydrate and not restrict H_2O transport from beneath.

Figure 12 provides the slab-surface CO_2 and H_2O flux profiles for the three-layer model with the various flow angles (θ). It shows that removal of the capping sediments leads to an overall increase of the CO_2 fluxes, and additionally to the emergence of a broad flux peak at the subarc depth range. In particular, when fluid flow is nearly up-slab (Figures 12k and 12l), the position of the flux peak coincides with the average position of global arc volcanoes projected onto slab surface (Syracuse and Abers, 2006). It is also interesting to compare between the flux profiles of the four-layer (Figure 12a) and three-layer models (Figure 12g), both with a flow angle of 90° : the carbonation reaction in the sedimentary layer clearly suppresses the CO_2 flux peak that would appear without it. Up-slab flows ($\theta > 90^\circ$) can therefore avoid the more reactive sediments at greater depths and eventually contribute to slab surface CO_2 fluxes. On the other hand, removal of the capping sediments does not increase the slab surface H_2O fluxes, except that it removes the flux dip at ~ 160 km in the four-layer reference model (Figure 12b). It is clear from our analysis of the open-system reference model (section 4.2) that the flux dip stems from porosity reduction due to enhanced carbonation in the sedimentary layer, thus the dip is eliminated after the removal of the sedimentary layer.

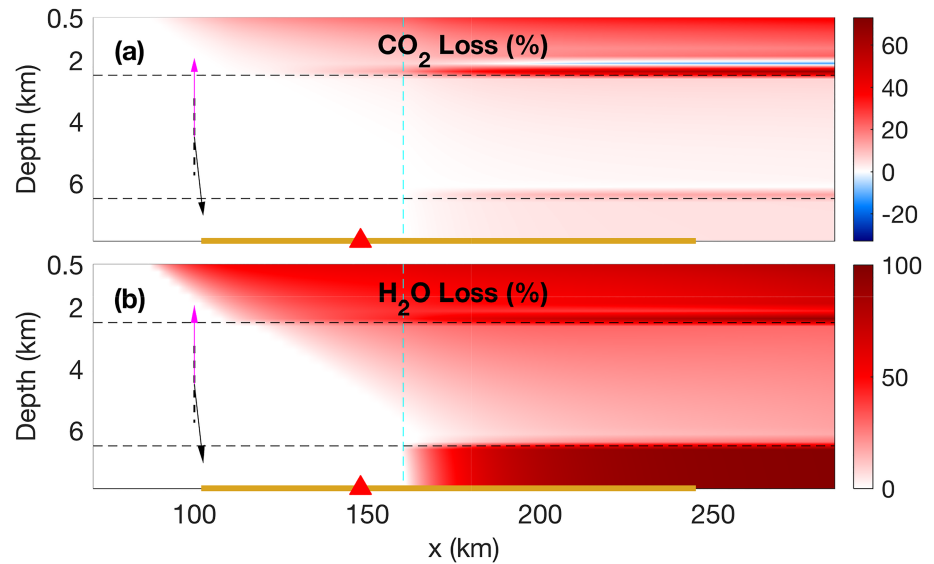


Figure 11. Volatile loss for the three-layer slab model with flow angle $\theta = 90^\circ$, that is, there is no capping sedimentary layer. Note that the depth starts from 0.5 km because the top replacement basaltic layer is excluded from calculation. (a) CO₂ loss; (b) H₂O loss.

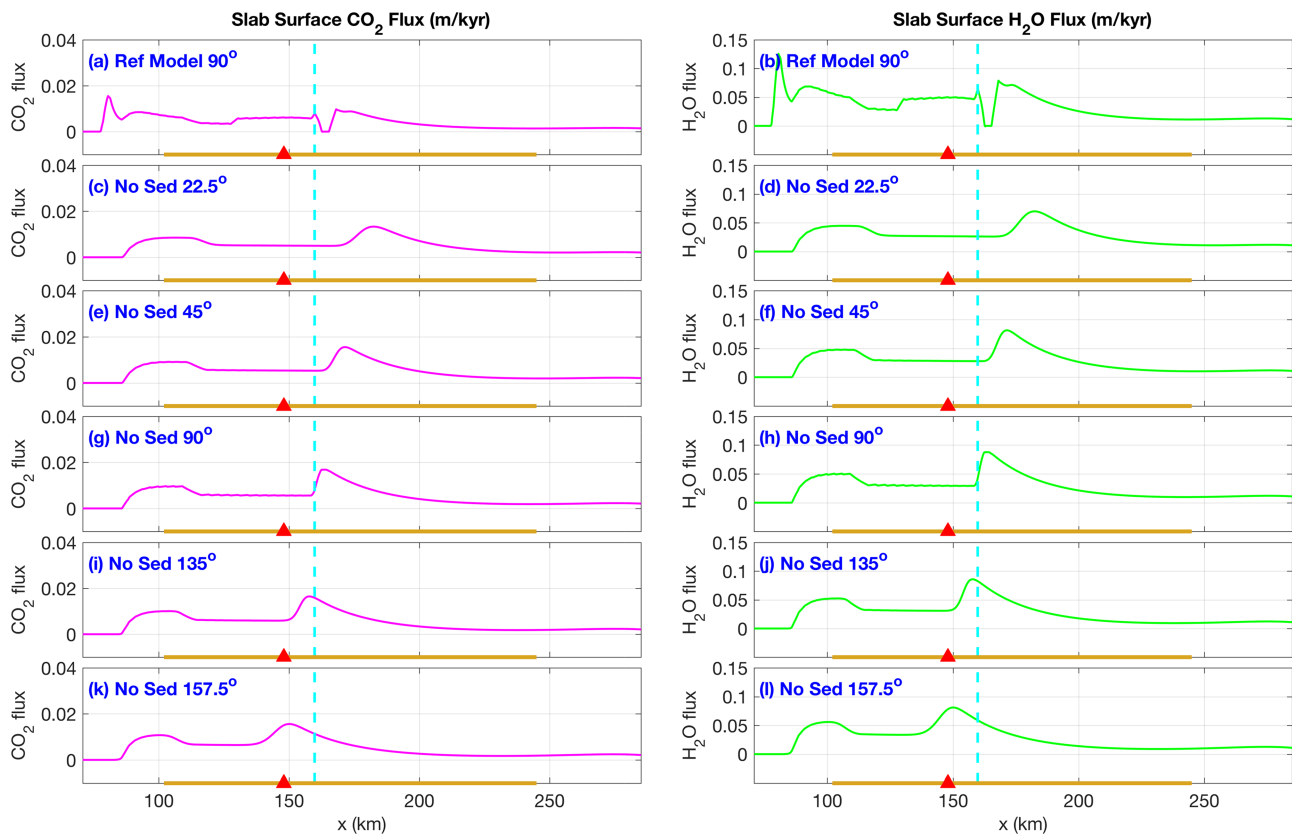


Figure 12. CO₂ (left panels: a, c, e, g, i and k) and H₂O (right panels: b, d, f, h, j and l) fluxes on the slab surface. Panels (a) and (b) are from the reference model that has a 500-m-thick sedimentary layer atop the slab, whereas the rest are results from the three-layer model with different flow angles (θ).

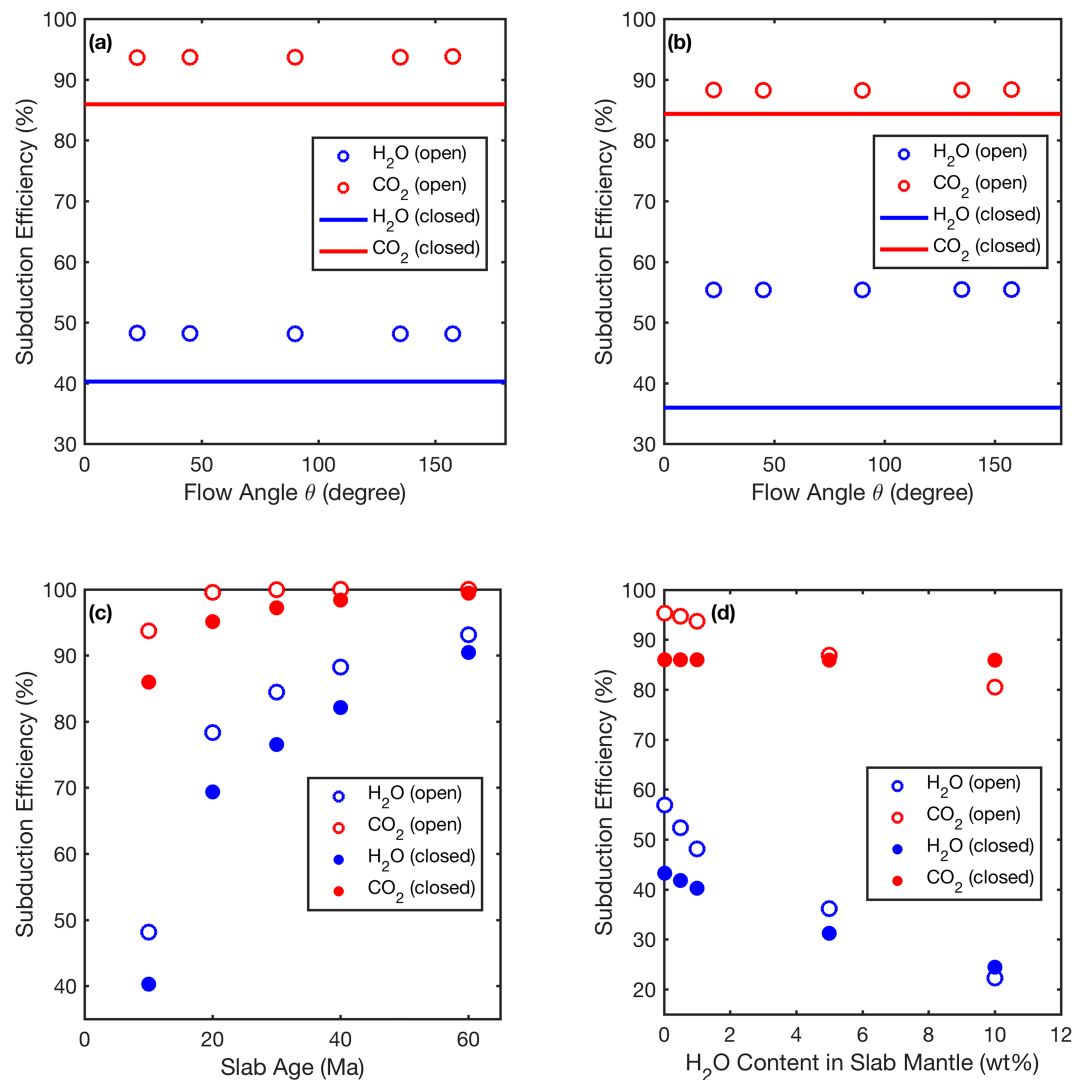


Figure 13. Subduction efficiency of H₂O (blue) and CO₂ (red). (a) Effect of flow angle θ , results extracted from sections 4.2 and 4.3. The closed-system subduction efficiencies do not depend on flow directions, so are plotted as lines. (b) Effect of flow angle θ , results extracted from the model without the top sedimentary layer in section 4.6. Same as in (a), the horizontal lines denote closed-system efficiencies. (c) Effect of slab age, results extracted from section 4.4. Open circles denote open-system results, whereas dots denote closed-system ones; same markers in (d). (d) Effect of the H₂O content in the hydrated slab upper mantle, results extracted from section 4.5.

The simplified three-layer model represents an end-member case where the subducted slab is devoid of sediments. By comparing the total CO₂ and H₂O amount in the three-layered slab with those in the four-layered slab in the reference model, we find that sediment removal causes ~11% CO₂ loss and ~9% H₂O loss from the slab. It is noteworthy that these estimates of CO₂ and H₂O loss via sediment removal do not account for the thermal effect resulted from the direct contact between the basalt layer and mantle wedge. Further heating of the basalt layer by mantle wedge can increase the CO₂ and H₂O loss from the slab, and thus their fluxes along the slab surface.

4.7. Subduction Efficiency of H₂O and CO₂

The subduction efficiency of H₂O (and CO₂) in this study is defined as the quotient of its total mass residing in the solid rock phase beyond ~200 km deep over that residing in the incoming slab. To demonstrate how the various factors in the preceding sections affect the subduction efficiency, we plot them in Figure 13.

Volatile redistribution among different layers shown in Figure 10 implies that the subduction efficiency for individual layers depends on flow direction; however, Figure 13a and 13b suggest that flow direction exerts

almost no influence on the subduction efficiency for the entire slab. Comparison between the open-system results in Figures 13a and 13b indicates that the subduction efficiency of CO_2 is reduced by $\sim 7\%$, due to the absence of a sedimentary layer where carbonation reaction can occur. Figure 13c illustrates that slab age strongly influences volatile subduction efficiency—the older the slab, the higher the efficiency. In particular, the 60 Ma cold slab is nearly 100% and 93% efficient in recycling CO_2 and H_2O beyond mantle depth of ~ 200 km. In addition, Figure 13d shows that the H_2O content of hydrated slab mantle exerts a much stronger control on the efficiency of volatile subduction. For extensively hydrated slab mantle (e.g., 10 wt% H_2O or $\sim 76\%$ serpentinization), the recycling efficiency of CO_2 can be reduced to $\sim 80\%$ and that of H_2O to as low as $\sim 21\%$.

Given that reactive flows are path dependent, the finding that the subduction efficiency in Figures 13a and 13b is insensitive to flow direction is surprising. However, it can be understood from the two assumptions in the model. The first is the local equilibrium assumption, which dictates that, as long as the P - T structure of the slab is constant, steady-state volatile production within the entire slab is determined by $\rho_s v_s \partial \phi / \partial z$ (see Appendix A). Since porosity ϕ further depends on bulk composition, which is affected by flow directions, in theory the volatile production ($\rho_s v_s \partial \phi / \partial z$) should be path dependent and thereby give rise to path dependence of subduction efficiency. However, changes in bulk H_2O and CO_2 content induced by varying flow direction are small and spatially limited such that the path dependence of subduction efficiency becomes indiscernible in Figures 13a and 13b. Thus, the flow angle (θ) shifts the volatile flux peaks, but not the overall amount of devolatilization. The second relevant model assumption is the uniform flow direction across slab, which makes strongly focused flows unlikely and hence prevents substantial alterations of bulk volatile content.

The subduction efficiency of H_2O has also been estimated by previous studies that do not consider CO_2 . For example, van Keken et al. (2011) estimate an average subduction efficiency of 32% for H_2O in the present-day subducting slabs. In their model, the basal slab mantle layer is 4 km thick and contains 2 wt% H_2O . In terms of the total amount of H_2O infiltration, this is roughly equivalent to a H_2O content of 5.3 wt% in the 1.5 km thick basal layer in our model. As shown in Figure 13d, our model would yield a H_2O subduction efficiency of $\sim 35\%$. Nonetheless, the average slab age in the model by van Keken et al. (2011) is older than 10 Ma that is adopted in the calculation for Figure 13d, implying that our model would yield a H_2O subduction efficiency higher than 35% for the present-day global subduction zones. The higher subduction efficiency of H_2O is expected because our model accounts for open-system effects. As demonstrated in Figure 13, the subduction efficiency of H_2O is generally higher in open-system models than in closed-system ones. This is mainly due to the fractionation-induced inhibition of H_2O loss in the bulk interior of subducted lithological layers (see section 4.2). Only in the case of strong infiltration in Figure 13d does the H_2O (and CO_2) subduction efficiency become lower in open systems than in closed systems. Similar to H_2O , CO_2 subduction efficiency is also elevated by open-system fractionation. Moreover, comparison between Figures 13a and 13b suggests that, for closed systems, removal of top sedimentary layer exerts almost no effect on the CO_2 subduction efficiency; however, for open systems, the CO_2 subduction efficiency is reduced by $\sim 7\%$ due to the sediment removal, highlighting again the importance of open-system effects.

5. Discussion

By treating the subducting slab as a nondeformable plate and assuming local equilibrium and uniform flow direction, our model solves for the steady-state reactive flows of H_2O and CO_2 and quantifies their fluxes from and storage within the slab. The merit of the model is its capability to couple open-system thermodynamics with fluid flow in a more realistic and consistent way. However, in achieving this capability, the choices made in model setup also impose limitations.

The first limitation lies in neglecting partial melting. Various studies have focused on the effects of H_2O on partial melting, and suggest that melting primarily occurs in the overlying mantle wedge due to solidus depression caused by slab-derived H_2O (Grove et al., 2006, 2012). Field studies in volcanic arc settings, however, discovered adakites that are interpreted to be evidence of slab melting in hot geotherms (Sen and Dunn, 1994; Drummond et al., 1996). When CO_2 is taken into account, experimental studies suggest that even in hot subduction zones, modern slab geotherms are still below the solidi of carbonated basalts and peri-

dotites and that only carbonated sediments are promising for carbonatite liberation (Dasgupta et al., 2013). On the other hand, Poli (2015) shows that partial melting of hydrous carbonated gabbros can produce carbonatitic liquids in warm subduction zones, as long as the gabbros are Ca-rich, a result likely from extensive hydrothermal alteration. In light of these experimental findings, neglecting the partial melting of slab mantle peridotite in our model is a reasonable choice, but ignoring the melting of mafic and sedimentary layers could overestimate the subduction efficiency of CO_2 , especially when migration of carbonatitic melt can remove considerable CO_2 from the slab. Moreover, absence of partial melts in the current model indicates that the thermal feedbacks from associated latent heat and melt transport is unaccounted for (Rees Jones et al., 2018). The influences of perturbation to the slab thermal structure caused by the loss of partial melts and/or sediments (section 4.6) need to be further assessed in future research.

The second limitation stems from the binary H_2O - CO_2 molecular fluids assumed for the liquid phase in our model. Variations of pressure, temperature and particularly oxygen fugacity during subduction can give rise to the dominance of methane (CH_4) or precipitation of graphite (Brovarone et al., 2017; Galvez et al., 2013). Moreover, ionic carbon species (e.g., HCO_3^- , CO_3^{2-}) are inferred to be common in subduction zone settings (Frezzotti et al., 2011; Ague and Nicolescu, 2014), although detailed thermodynamic modeling suggests that molecular carbon species can dominate over ionic ones in fluids derived from subducted basalts (Galvez et al., 2016) and sediments (Connolly and Galvez, 2018). The latter study also shows that potassium in ionic form can be depleted from the slab-top sediments, destabilizing hydrous phases like micas and thus facilitating volatile release. In addition to potassium, the activity of dissolved silica and aluminum also affects the stability of silicates that participate in carbonate dissolution reactions (Galvez and Pubellier, 2019). Therefore, omission of the direct contribution from carbon species other than CO_2 and indirect contribution from dissolved nonvolatile elements (e.g., Si and Al) might underestimate the water and carbon fluxes from the slab, and in turn overestimate their recycling efficiency.

The third limitation arises from the assumption of uniform flow direction. As explained in section 2 on the model setup, choosing the flow direction θ as a free parameter enables the model to explore the variation of general patterns of within-slab flows predicted by various dynamic models; however, it suffers from losing the details of flow dynamics within the slab. In particular, the strong flow focusing, widely documented in the field (Ague, 2007; Barnicoat and Cartwright, 1995; Breeding et al., 2003; Philippot and Selverstone, 1991; Piccoli et al., 2016; Piccoli et al., 2018), and predicted by dynamic models (Faccenda et al., 2009; Malvoisin et al., 2015; Plümper et al., 2017; Wilson et al., 2014), cannot be simulated in the current model. As demonstrated by Wada et al. (2012), heterogeneous hydration associated with local flow focusing can promote H_2O release and reduce its subduction efficiency. Therefore, further work remains to incorporate dynamics into the open-system flow model to evaluate how flow focusing can affect the slab surface fluxes of CO_2 and H_2O , and their recycling efficiency by subduction.

The fourth limitation relates to the assumption of no compaction in the slab. To assess the effect of compaction, we compare the magnitude of fluid fluxes in our reference model with that in the compaction model by Wilson et al. (2014). Our slab model (section 4.2) initially contains ~ 2.60 wt% H_2O on average, yielding a maximum surface flux of ~ 0.1 m/kyr (Figure 6f). In contrast, the compaction model initially contains ~ 1.85 wt% H_2O on average, yielding a maximum surface flux of ~ 0.8 m/kyr. Taken at face value, the compaction model generates a flux that is eight times larger than that from our non-compaction model. However, as shown in Figure 5b, the H_2O flux drop in our reference model is caused not only by neglecting compaction, but also by the open-system fractionation, which can account for up to $\sim 70\%$ of the flux drop. If this open-system effect were considered by Wilson et al. (2014), the magnitude of H_2O fluxes in their model would become comparable to that in our reference model, indicating that the influence of compaction is insignificant with respect to the magnitude of slab surface fluxes. Nevertheless, as stressed above, compaction may be important if it is a control on fluid flow pathways within the slab.

In interpreting our model results on the slab surface fluxes, an additional assumption is made that magmas produced by flux melting of the mantle wedge traverse the wedge vertically without any lateral deflection to feed arc volcanoes. It follows that, if the average position of global arc volcanoes is projected downward onto the slab surface, it should correspond to a peak in slab surface flux. It is under this assumption that the up-slab flows in Figure 6 are necessary to produce the melt feeding arc volcanism. However, two-phase geodynamic models of the mantle wedge suggest that the melt and fluid transport through the wedge is more complex than simply vertical, and depends on many factors including solid rheology and grain size

in the wedge (Cerpa et al., 2017, 2018; Wilson et al., 2014). In addition, the coincidence of flux peaks and the projected volcanic arc position in Figures 6 and 12 is premised on the hot thermal structure of the 10 Ma slab. As demonstrated in Figures 8 and 9, an old slab shifts the flux peak to greater depths, and higher hydration extent of the slab base shifts the peak to shallower depths. Since a slower convergence rate leads to a warmer subducting slab (Penniston-Dorland et al., 2015), it can be expected that the position of the flux peak also varies with convergence rate. How the shift in flux-peak position influences the dynamics of melt or volatile transport in the wedge, and eventually the genesis of arc magmas, remains to be explored by future models that include both the dynamics and thermodynamics in the wedge.

6. Conclusion

In summary, we assess the controlling factors for CO_2 and H_2O release from subducting slabs. We find that up-slab flows are necessary to form a flux peak at subarc depths, which could be responsible for the magmatic genesis of arc volcanoes if the flux-induced melts traverse the mantle wedge vertically. Such a result aligns with the findings of dynamic studies by Wilson et al. (2014) where a flow channel is formed to induce up-slab flows. Sufficiently hydrated slab mantle can relax the above requirement for flow directions, but when the slab mantle is additionally carbonated, the onset position of its devolatilization becomes deeper, still making up-slab flows important for supplying maximum volatile release at subarc depths. Moreover, H_2O infiltration from dehydrating slab mantle can mobilize CO_2 in the overlying gabbroic and basaltic layers, but only redistribute the carbon to the slab surface sediments where significant carbonation takes place. The subducting sediments, if passing the accretionary prism and surviving diapiric removal and partial melting, can be an important barrier to CO_2 liberation from slabs. Conversely, loss or partial melting of the sediments can be crucial avenues for CO_2 transfer from subducting slab to mantle wedge. The subduction efficiency of H_2O is $\sim 20\text{--}90\%$ in our model, generally higher than that in previous closed-system models that consider only H_2O . The CO_2 subduction efficiency is $\sim 80\text{--}100\%$. The higher volatile subduction efficiency compared to closed-system models stems from the open-system fractionation effect that inhibits overall devolatilization in the interior of lithological layers. The absolute values are likely overestimates because the effects of flow focusing and fluid species other than H_2O and CO_2 are ignored in the model, which should be considered in future studies.

Appendix A

At steady state, the fluid fluxes can be calculated according to equation (5) that further reduces to:

$$\rho_f \nabla \cdot (\mathbf{v}_f \phi) = \rho_s \mathbf{v}_s \cdot \nabla \phi. \quad (\text{A1})$$

Figure A1 shows part of the numerical grid established on the slab coordinate system (Figure 1b), where the fluid fluxes $F = v_f \phi$ can then be expressed through integration along flow path (l):

$$F = \int_{\text{path start}}^{\text{path end}} \frac{\rho_s}{\rho_f} v_s \frac{\partial \phi}{\partial x} dl. \quad (\text{A2})$$

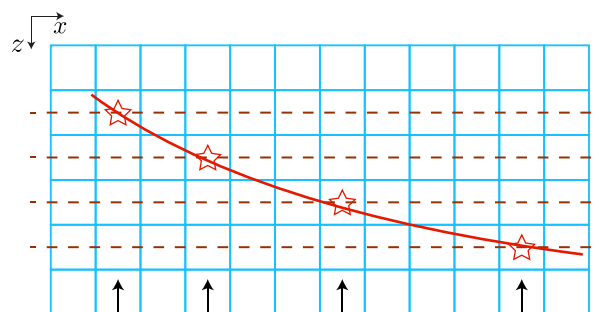


Figure A1. An illustrative part of the numerical grid in this study. Stars mark the position where onset of devolatilization occurs at relevant slab depths, and the connecting red solid line is the envelope for devolatilization onset within the slab. Brown dashed lines are iso-depth traverses along which $\partial \phi / \partial x$ will be plotted in Figure A2a, and black arrows denote the direction of flux integration for the reference model ($\theta = 90^\circ$).

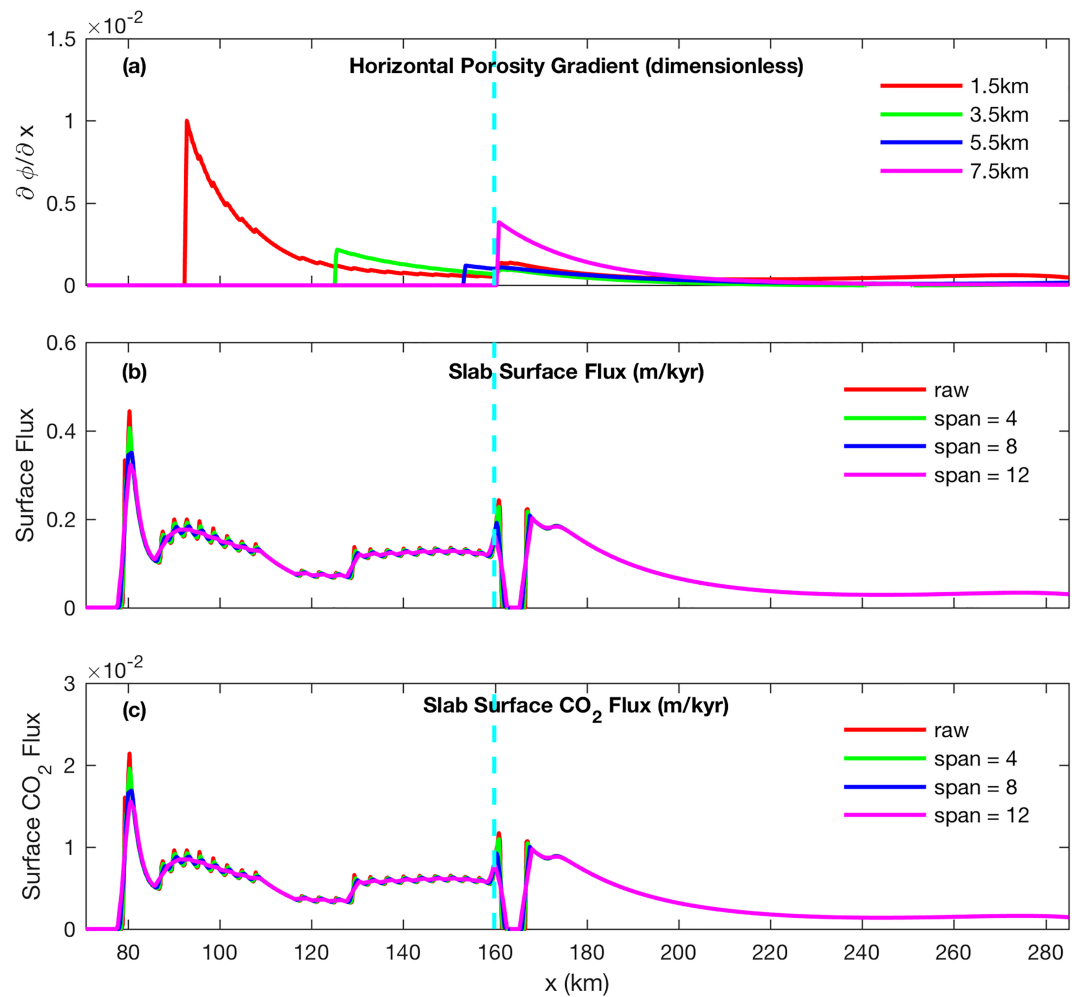


Figure A2. (a). Profiles of $\partial\phi/\partial x$ that contributes to fluid fluxes. Different line colors are used to distinguish the depths at which these profiles are extracted from the open-system reference model in section 4.2. (b). Slab surface fluxes from the reference model. Red line denotes the raw model result that shows flux fluctuations, whereas other lines represent the model result smoothed to different extent. The “span” here means the number of neighboring grid points used for averaging the flux at a specific grid point. The spacing between grid points in the model is 250 m, so a span of 12 corresponds to an averaging window width of 3 km. (c). Same as in (b), but is for slab surface CO_2 flux. Vertical dashed lines mark the onset of dehydration for slab lithospheric mantle.

For the reference model with flow direction $\theta = 90^\circ$, flow paths are perpendicular to the slab, so the integration is along the z -axis direction in Figure A1. At any specific depth (dashed lines in Figure A1), the onset of devolatilization leads to an abrupt elevation of porosity (ϕ) and thus a pulse in the $\partial\phi/\partial x$ profile along the iso-depth traverse. Figure A2 shows the $\partial\phi/\partial x$ and flux profiles along various iso-depth traverses of the modeled slab, and Figure A2a illustrates that the pulses in $\partial\phi/\partial x$ appear at different horizontal positions within the slab. According to equation (A2), when flow trajectories pass the locations of the pulses, the calculated fluid fluxes will inherit these pulses. For the reference model where flow paths are normal to x -axis and the pulses are horizontally apart from one another (Figure A1), the inherited pulses lead to the fluctuation in the fluid flux distribution (Figures A2b, A2c, and 4g). Beyond the slab distance ~ 160 km where the basal slab mantle dehydrates, the envelope of the onset of devolatilization (red solid line in Figure A1) is surpassed, so there are no pulses in $\partial\phi/\partial x$ at any depth. The flux fluctuations disappear accordingly as in Figure A2b–c and Figure 4h.

The analysis above indicates that refining numerical grid will produce more but weaker fluctuations in slab surface fluxes before ~ 160 km, but the trend and main features of flux profiles stay unchanged. To focus on the general trend and main features, we smooth the flux profiles by averaging over a span of neighboring

grid points. As illustrated in Figures A2b and A2c, smoothing with a span of 12 grid points (3 km) well preserves the flux trend and features, so it is applied to all the slab surface flux profiles in this study.

Acknowledgments

We thank the three anonymous reviewers for their comments that helped us improve this paper. We thank the Isaac Newton Institute for Mathematical Sciences for holding the Melt in the Mantle program sponsored by EPSRC Grant EP/K032208/1. Support from Deep Carbon Observatory funded by the Sloan Foundation is acknowledged. M. T. acknowledges the Royal Society Newton International Fellowship (NF150745). D. R. J. acknowledges research funding through the NERC Consortium Grant NE/M000427/1, NERC Standard Grant NE/I026995/1, and the Leverhulme Trust. This project has also received funding from the European Research Council (ERC) under the European Union's Horizon 2020 research and innovation program (Grant Agreement 772255). This contribution is about numerical modeling, so it does not depend on experimental or field data. Relevant data and equations for reproducing the model results are already contained in the text. Nonetheless, we provide an example code on the usage of the thermodynamic parameterization: https://bitbucket.org/meng_tian/example_code_thermo_module/src/master/.

References

- Ague, J. J. (2007). Models of permeability contrasts in subduction zone melange: Implications for gradients in fluid fluxes, Syros and Tinos islands Greece. *Chemical Geology*, 239(3-4), 217–227. <https://doi.org/10.1016/j.chemgeo.2006.08.012>
- Ague, J. J., & Nicolescu, S. (2014). Carbon dioxide released from subduction zones by fluid-mediated reactions. *Nature Geoscience*, 7(5), 355–360. <https://doi.org/10.1038/NGEO2143>
- Balay, S., Abhyankar, S., Adams, M. F., Brown, J., Brune, P., Buschelman, K., Zhang, H. (2018). PETSc Web page. <http://www.mcs.anl.gov/petsc>.
- Barnicoat, A. C., & Cartwright, I. (1995). Focused-flow during subduction: Oxygen isotope data from high-pressure ophiolites of the Western Alps. *Earth and Planetary Science Letters*, 132(1-4), 53–61.
- Behn, M. D., Kelemen, P. B., Hirth, G., Hacker, B. R., & Massonne, H.-J. (2011). Diapirs as the source of the sediment signature in arc lavas. *Nature Geoscience*, 4(9), 641–646. <https://doi.org/10.1038/ngeo1214>
- Breeding, C. M., Ague, J. J., & Bröcker, M. (2004). Fluid-metasedimentary rock interactions in subduction-zone élange: Implications for the chemical composition of arc magmas. *Geology*, 32(12), 1041–1044.
- Breeding, C. M., Ague, J. J., Brocker, M., & Bolton, E. W. (2003). Blueschist preservation in a retrograded, high-pressure, low-temperature metamorphic terrane, Tinos Greece: Implications for fluid flow paths in subduction zones. *Geochemistry, Geophysics, Geosystems*, 4(9002), 1–13. <https://doi.org/10.1029/2002GC000380>
- Brovarone, A. V., & Beyssac, O. (2014). Lawsonite metasomatism: A new route for water to the deep earth. *Earth and Planetary Science Letters*, 393, 275–284.
- Brovarone, A. V., Martinez, I., Elmaleh, A., Compagnoni, R., Chaduteau, C., & Ferraris, C., & Esteve, I. (2017). Massive production of abiotic methane during subduction evidenced in metamorphosed ophiocarbonates from the Italian Alps. *Nature Communications*, 8, 14134.
- Carlson, R. L. (2003). Bound water content of the lower oceanic crust estimated from modal analyses and seismic velocities of oceanic diabase and gabbro. *Geophysical Research Letters*, 30(22), 2142. <https://doi.org/10.1029/2003GL018213>
- Carlson, R. L., & Miller, D. J. (2003). Mantle wedge water contents estimated from seismic velocities in partially serpentinized peridotites. *Geophysical Research Letters*, 30(5), 1250. <https://doi.org/10.1029/2002GL016600>
- Cerpa, N. G., Wada, I., & Wilson, C. R. (2017). Fluid migration in the mantle wedge: Influence of mineral grain size and mantle compaction. *Journal of Geophysical Research: Solid Earth*, 122, 6247–6268. <https://doi.org/10.1002/2017JB014046>
- Cerpa, N. G., Wada, I., & Wilson, C. R. (2018). Effects of fluid influx, fluid viscosity, and fluid density on fluid migration in the mantle wedge and their implications for hydrous melting. *Geosphere*, 15(1), 1–23.
- Connolly, J. A. D., & Galvez, M. E. (2018). Electrolytic fluid speciation by Gibbs energy minimization and implications for subduction zone mass transfer. *Earth and Planetary Science Letters*, 501, 90–102.
- Dasgupta, R., Hazen, R. M., Jones, A. P., & Baross, J. A. (2013). Ingassing, storage, and outgassing of terrestrial carbon through geologic time. *Reviews in Mineralogy and Geochemistry*, 75, 183–229. <https://doi.org/10.2138/rmg.2013.75.7>
- Dasgupta, R., & Hirschmann, M. M. (2010). The deep carbon cycle and melting in Earth's interior. *Earth and Planetary Science Letters*, 298(1-2), 1–13. <https://doi.org/10.1016/j.epsl.2010.06.039>
- Drummond, M. S., Defant, M. J., & Kepezhinskas, P. K. (1996). Petrogenesis of slab-derived trondhjemite-tonalite-dacite/adakite magmas. *Transactions of the Royal Society of Edinburgh Earth Sciences*, 87, 205–215.
- England, P. C., & Katz, R. F. (2010). Melting above the anhydrous solidus controls the location of volcanic arcs. *Nature*, 467(7316), 700–U84. <https://doi.org/10.1038/nature09417>
- Faccenda, M., Gerya, T. V., & Burlini, L. (2009). Deep slab hydration induced by bending-related variations in tectonic pressure. *Nature Geoscience*, 2(11), 790–793. <https://doi.org/10.1038/NGEO656>
- Frezza, M. L., Selverstone, J., Sharp, Z. D., & Compagnoni, R. (2011). Carbonate dissolution during subduction revealed by diamond-bearing rocks from the Alps. *Nature Geoscience*, 4(10), 703–706. <https://doi.org/10.1038/NGEO1246>
- Früh-Green, G. L., Connolly, J. A., Plas, A., Kelley, D. S., & Grobety, B. (2004). Serpentinization of oceanic peridotites: Implications for geochemical cycles and biological activity. In W. S. Wilcock, E. F. Delong, D. S. Kelley, J. A. Baross, & S. Craig Cary (Eds.), *The seafloor biosphere at mid-ocean ridges*, AGU Geophysical Monograph Series (Vol. 144, pp. 119–136). Hoboken, NJ: John Wiley & Sons Inc. <https://doi.org/10.1029/144GM08>
- Galvez, M. E., Connolly, J. A., & Manning, C. E. (2016). Implications for metal and volatile cycles from the pH of subduction zone fluids. *Nature*, 539(7629), 420.
- Galvez, M. E., Martinez, I., Beyssac, O., Benzerara, K., Agrinier, P., & Assayag, N. (2013). Metasomatism and graphite formation at a lithological interface in Malaspinga (Alpine Corsica, France). *Contributions to Mineralogy and Petrology*, 166(6), 1687–1708.
- Galvez, M. E., & Pubellier, M. (2019). How do subduction zones regulate the carbon cycle? In B. N. Orcutt, I. Daniel, & R. Dasgupta (Eds.), *Deep Carbon: Past to Present* (pp. 276–312). Cambridge: Cambridge University Press.
- Garth, T., & Rietbrock, A. (2014). Order of magnitude increase in subducted H₂O due to hydrated normal faults within the Wadati-Benio zone. *Geology*, 42(3), 207–210. <https://doi.org/10.1130/G34730.1>
- Garth, T., & Rietbrock, A. (2017). Constraining the hydration of the subducting Nazca plate beneath Northern Chile using subduction zone guided waves. *Earth and Planetary Science Letters*, 474, 237–247. <https://doi.org/10.1016/j.epsl.2017.06.041>
- Gerya, T. (2011). Future directions in subduction modeling. *Journal of Geodynamics*, 52(5), 344–378.
- Gorman, P. J., Kerrick, D. M., & Connolly, J. A. D. (2006). Modeling open system metamorphic decarbonation of subducting slabs. *Geochemistry, Geophysics, Geosystems*, 7, Q04007. <https://doi.org/10.1029/2005GC001125>
- Grevemeyer, I., Ranero, C. R., Flueh, E. R., Klaeschen, D., & Bialas, J. (2007). Passive and active seismological study of bending-related faulting and mantle serpentinization at the Middle America trench. *Earth and Planetary Science Letters*, 258(3-4), 528–542. <https://doi.org/10.1016/j.epsl.2007.04.013>
- Grove, T. L., Chatterjee, N., Parman, S. W., & Medard, E. (2006). The influence of H₂O on mantle wedge melting. *Earth and Planetary Science Letters*, 249(1-2), 74–89. <https://doi.org/10.1016/j.epsl.2006.06.043>
- Grove, T. L., Till, C. B., Krawczynski, M. J., & Jeanloz, R. (2012). The role of H₂O in subduction zone magmatism. *Annual Review of Earth and Planetary Sciences*, 40, 413–439. <https://doi.org/10.1146/annurev-earth-042711-105310>

- Hacker, B. R. (2008). H₂O subduction beyond arcs. *Geochemistry, Geophysics, Geosystems*, 9, Q03001. <https://doi.org/10.1029/2007GC001707>
- Hacker, B. R., Abers, G. A., & Peacock, S. M. (2003). Subduction factory: 1. Theoretical mineralogy, densities, seismic wave speeds, and H₂O contents. *Journal of Geophysical Research*, 108(B1), 2029. <https://doi.org/10.1029/2001JB001127>
- Hart, S. R., & Zindler, A. (1986). In search of a bulk-Earth composition. *Chemical Geology*, 57(3-4), 247–267.
- Hirschmann, M. M. (2018). Comparative deep Earth volatile cycles: The case for C recycling from exosphere/mantle fractionation of major (H₂O, C, N) volatiles and from H₂O/Ce, CO₂/Ba, and CO₂/Nb exosphere ratios. *Earth and Planetary Science Letters*, 502, 262–273.
- Katz, R. F. (2008). Magma dynamics with the enthalpy method: Benchmark solutions and magmatic focusing at mid-ocean ridges. *Journal of Petrology*, 49(12), 2099–2121. <https://doi.org/10.1093/petrology/egn058>
- Katz, R. F., Knepley, M. G., Smith, B., Spiegelman, M., & Coon, E. T. (2007). Numerical simulation of geodynamic processes with the portable extensible toolkit for scientific computation. *Physics of the Earth and Planetary Interiors*, 163(1-4), 52–68. <https://doi.org/10.1016/j.pepi.2007.04.016>
- van Keken, P. E., Currie, C., King, S. D., Behn, M. D., Cagnioncle, A., He, J., et al. (2008). A community benchmark for subduction zone modeling. *Physics of the Earth and Planetary Interiors*, 171(1-4), 187–197. <https://doi.org/10.1016/j.pepi.2008.04.015>
- van Keken, P. E., Hacker, B. R., Syracuse, E. M., & Abers, G. A. (2011). Subduction factory: 4. depth-dependent flux of H₂O from subducting slabs worldwide. *Journal of Geophysical Research*, 116, B01401. <https://doi.org/10.1029/2010JB007922>
- Kelemen, P. B., & Manning, C. E. (2015). Reevaluating carbon fluxes in subduction zones, what goes down, mostly comes up. *Proceedings of the National Academy of Sciences of the United States of America*, 112(30), E3997–E4006. <https://doi.org/10.1073/pnas.1507889112>
- Keller, T., & Katz, R. F. (2016). The role of volatiles in reactive melt transport in the asthenosphere. *Journal of Petrology*, 57(6), 1073–1108. <https://doi.org/10.1093/petrology/egw030>
- Kerrick, D. M. (2002). Serpentine seduction. *Science*, 298(5597), 1344–1345.
- Kerrick, D. M., & Connolly, J. A. D. (1998). Subduction of ophiocarbonates and recycling of CO₂ and H₂O. *Geology*, 26(4), 375–378.
- Kerrick, D. M., & Connolly, J. A. D. (2001a). Metamorphic devolatilization of subducted marine sediments and the transport of volatiles into the Earth's mantle. *Nature*, 411(6835), 293–296.
- Kerrick, D. M., & Connolly, J. A. D. (2001b). Metamorphic devolatilization of subducted oceanic metabasalts: Implications for seismicity, arc magmatism and volatile recycling. *Earth and Planetary Science Letters*, 189(1-2), 19–29.
- Malvoisin, B., Podladchikov, Y. Y., & Vrijmoed, J. C. (2015). Coupling changes in densities and porosity to fluid pressure variations in reactive porous fluid flow: Local thermodynamic equilibrium. *Geochemistry, Geophysics, Geosystems*, 16, 4362–4387. <https://doi.org/10.1002/2015GC006019>
- Marshall, H. R., & Schumacher, J. C. (2012). Arc magmas sourced from éelange diapirs in subduction zones. *Nature Geoscience*, 5, 862–867.
- McKenzie, D. (1984). The generation and compaction of partially molten rock. *Journal of Petrology*, 25(3), 713–765.
- Morishige, M., & van Keken, P. E. (2018). Fluid migration in a subducting viscoelastic slab. *Geochemistry, Geophysics, Geosystems*, 19, 337–355. <https://doi.org/10.1002/2017GC007236>
- Paulatto, M., Laigle, M., Galve, A., Charvis, P., Sapin, M., Bayrakci, G., et al. (2017). Dehydration of subducting slow-spread oceanic lithosphere in the Lesser Antilles. *Nature Communications*, 8, 15980. <https://doi.org/10.1038/ncomms15980>
- Peacock, S. M. (1990). Fluid processes in subduction zones. *Science*, 248(4953), 329–337.
- Peacock, S. M. (1991). Numerical simulation of subduction zone pressure-temperature-time paths: Constraints on fluid production and arc magmatism. *Philosophical Transactions of the Royal Society A-Mathematical Physical and Engineering Sciences*, 335(1638), 341–353.
- Peacock, S. M. (2001). Are the lower planes of double seismic zones caused by serpentine dehydration in subducting oceanic mantle? *Geology*, 29(4), 299–302.
- Penniston-Dorland, S. C., Kohn, M. J., & Manning, C. E. (2015). The global range of subduction zone thermal structures from exhumed blueschists and eclogites: Rocks are hotter than models. *Earth and Planetary Science Letters*, 428, 243–254. <https://doi.org/10.1016/j.epsl.2015.07.031>
- Philippot, P., & Selverstone, J. (1991). Trace-element-rich brines in eclogitic veins: Implications for fluid composition and transport during subduction. *Contributions to Mineralogy and Petrology*, 106(4), 417–430.
- Piccoli, F., Brovarone, A. V., & Ague, J. J. (2018). Field and petrological study of metasomatism and high-pressure carbonation from lawsonite eclogite-facies terrains, alpine corsica. *Lithos*, 304–307, 16–37. <https://doi.org/10.1016/j.lithos.2018.01.026>
- Piccoli, F., Brovarone, A. V., Beyssac, O., Martinez, I., Ague, J. J., & Chaduteau, C. (2016). Carbonation by fluid-rock interactions at high-pressure conditions: Implications for carbon cycling in subduction zones. *Earth and Planetary Science Letters*, 445, 146–159. <https://doi.org/10.1016/j.epsl.2016.03.045>
- Plank, T., & Langmuir, C. H. (1998). The chemical composition of subducting sediment and its consequences for the crust and mantle. *Chemical Geology*, 145(3-4), 325–394.
- Plümper, O., John, T., Podladchikov, Y. Y., Vrijmoed, J. C., & Scambelluri, M. (2017). Fluid escape from subduction zones controlled by channel-forming reactive porosity. *Nature Geoscience*, 10(2), 150–156. <https://doi.org/10.1038/NGEO2865>
- Poli, S. (2015). Carbon mobilized at shallow depths in subduction zones by carbonatitic liquids. *Nature Geoscience*, 8, 633–637.
- Putlitz, B., Matthews, A., & Valley, J. W. (2000). Oxygen and hydrogen isotope study of high-pressure metagabbros and metabasalts (Cyclades, Greece): Implications for the subduction of oceanic crust. *Contributions to Mineralogy and Petrology*, 138(2), 114–126.
- Ranero, C. R., Morgan, J. P., McIntosh, K., & Reichert, C. (2003). Bending-related faulting and mantle serpentinization at the Middle America trench. *Nature*, 425(6956), 367–373. <https://doi.org/10.1038/nature01961>
- Raymond, L. A. (2019). Perspectives on the roles of melanges in subduction accretionary complexes: A review. *Gondwana Research*, 74, 68–89.
- Rees Jones, D. W., Katz, R. F., Tian, M., & Rudge, J. F. (2018). Thermal impact of magmatism in subduction zones. *Earth and Planetary Science Letters*, 481, 73–79. <https://doi.org/10.1016/j.epsl.2017.10.015>
- Rüpke, L. H., Morgan, J. P., Hort, M., & Connolly, J. A. D. (2004). Serpentine and the subduction zone water cycle. *Earth and Planetary Science Letters*, 223(1-2), 17–34. <https://doi.org/10.1016/j.epsl.2004.04.018>
- Scott, D. R., & Stevenson, D. J. (1986). Magma ascent by porous flow. *Journal of Geophysical Research*, 91(B9), 9283–9296.
- Sen, C., & Dunn, T. (1994). Dehydration melting of a basaltic composition amphibolite at 1.5 and 2.0 GPa: Implications for the origin of adakites. *Contributions to Mineralogy and Petrology*, 117(4), 394–409.
- Seno, T., & Yamanaka, Y. (1996). Double seismic zones, compressional deep trench-outer rise events, and superplumes. In G. E. Bebout, D. W. Scholl, S. H. Kirby, & J. P. Platt (Eds.), *Subduction: Top to Bottom*, AGU Geophysical Monograph Series (Vol. 96, pp. 347–355). Hoboken, NJ: John Wiley & Sons Inc. <https://doi.org/10.1029/GM096p0347>
- Shimoda, G., & Kogiso, T. (2019). Effect of serpentine dehydration in subducting slabs on isotopic diversity in recycled oceanic crust and its role in isotopic heterogeneity of the mantle. *Geochemistry, Geophysics, Geosystems*. <https://doi.org/10.1029/2019GC008336>

- Sverjensky, D. A., Stagno, V., & Huang, F. (2014). Important role for organic carbon in subduction-zone fluids in the deep carbon cycle. *Nature Geoscience*, 7(12), 909–913. <https://doi.org/10.1038/NGEO2291>
- Syracuse, E. M., & Abers, G. A. (2006). Global compilation of variations in slab depth beneath arc volcanoes and implications. *Geochemistry, Geophysics, Geosystems*, 7, Q05017. <https://doi.org/10.1029/2005GC001045>
- Tian, M., Katz, R. F., & Rees Jones, D. W. (2019). Devolatilization of Subducting Slabs, Part I: Thermodynamic parameterization and open system effects. *Geochemistry, Geophysics, Geosystems*, 20. <https://doi.org/10.1029/2019GC008488>
- Wada, I., Behn, M. D., & Shaw, A. M. (2012). Effects of heterogeneous hydration in the incoming plate, slab rehydration, and mantle wedge hydration on slab- derived H₂O flux in subduction zones. *Earth and Planetary Science Letters*, 353, 60–71. <https://doi.org/10.1016/j.epsl.2012.07.025>
- Wilson, C. R., Spiegelman, M., van Keken, P. E., & Hacker, B. R. (2014). Fluid flow in subduction zones: The role of solid rheology and compaction pressure. *Earth and Planetary Science Letters*, 401, 261–274. <https://doi.org/10.1016/j.epsl.2014.05.052>